Int. J. Advanced Design and Manufacturing Technology, 2024, Vol. 17, No. 4, pp. 1-9

DOI: ***ISSN: 2252-0406*** ***https://admt.isfahan.iau.ir***

Innovative Enhancements in Surface Quality and Hardness of Aluminium Alloy 2024 through an Optimized Burnishing Process

Akbar Hojjati Najafabadi*
Department of Mechanical Engineering,
Mobarakeh branch, Islamic Azad University, Isfahan, Iran
E-mail: ak.hojjati@iau.ac.ir
*Corresponding author

Received: 22 July 2024, Revised: 9 October 2024, Accepted: 2 November 2024

Abstract: The burnishing process showcases a novel approach for significantly improving the surface quality and hardness of metals, particularly aluminium, copper, and brass. This paper presents a novel approach to optimize the burnishing process of Aluminium 2024 by simultaneously analyzing the effects of spindle speed, feed rate, and burnishing force, a comprehensive method that has not been addressed in prior studies. Utilizing a specially designed roller-based tool with a lathe machine, we systematically varied key parameters—spindle speed, feed rate, and burnishing force—through a full factorial design with two repetitions. Advanced statistical analysis was conducted using Minitab software to assess the effects of these parameters on surface roughness and hardness, employing regression methods for precise predictions. Remarkably, the results demonstrated that optimal surface roughness (Ra = 0.05 μm) was attained at a feed rate of 0.11 mm/rev, spindle speed of 1000 r/min, and burnishing force of 1000 N. This research not only highlights the effectiveness of the burnishing process in enhancing the mechanical properties of aluminium alloys but also introduces innovative methodologies that pave the way for improved industrial applications. Future studies will investigate the effects of burnishing in corrosive environments and its impact on material strength.

Keywords: Aluminium Alloy 2024, Burnishing Process, Mechanical Properties, Statistical Analysis, Surface Quality

Biographical notes: Akbar Hojjati Najafabadi received his PhD in Mechanical and Manufacturing Engineering from Kashan University, Iran, in 2020. He is an assistant professor at the Islamic Azad University, Mobarakeh branch. His research interests include robotics and wearable devices, assistive robotics, the development of innovative mechanical systems in rehabilitation, and manufacturing processes.

Research paper

1 INTRODUCTION

The demand for advanced materials with enhanced mechanical properties and superior surface characteristics continues to grow in various industries, particularly in aerospace, automotive, and manufacturing sectors. Aluminium Alloy 2024, known for its high strength-to-weight ratio and excellent fatigue resistance, has become a preferred choice in applications where performance and durability are paramount [1]. Components made from this alloy are frequently subjected to rigorous conditions, making their surface quality and hardness critical factors in ensuring longevity and reliability.

Importance of Surface Quality and Hardness

Surface quality plays a crucial role in determining the overall performance of engineering components. It influences not only the aesthetic appeal of the finished product but also its mechanical properties, including wear resistance, fatigue strength, and corrosion resistance. A smooth surface finish can significantly reduce friction and wear, leading to prolonged service life and improved efficiency [2]. Conversely, poor surface quality can result in premature failure of components, increased maintenance costs, and reduced operational efficiency. In this study, several key parameters are crucial for understanding the burnishing process of Aluminium 2024. Spindle speed refers to the rotational speed of the tool or workpiece, typically measured in revolutions per minute (rpm). The feed rate is defined as the distance that the tool advances during one complete revolution, expressed in millimeters per revolution (mm/rev). Lastly, burnishing force is the force exerted by the burnishing tool against the workpiece, measured in newtons (N). Understanding these terms is essential for comprehending the methodology and results presented in this paper. Hardness, on the other hand, is a measure of a material's resistance to deformation and wear. Increased hardness often correlates with enhanced wear resistance, making it a desirable characteristic for components subjected to high loads and abrasive environments [3]. Consequently, optimizing both surface quality and hardness is essential for achieving high-performance standards in applications involving Aluminium Alloy 2024.

Traditional Surface Finishing Techniques

Traditional surface finishing methods, such as grinding, honing, and polishing, have been widely used to improve surface quality. Each of these techniques has its advantages and limitations. For instance, grinding is effective for removing material and achieving precise dimensions, but it can introduce surface defects and residual stresses that may compromise material performance [4]. Honing is suitable for achieving high geometric accuracy but can be time-consuming and costly [5]. Polishing, while capable of producing a mirror-like finish, often requires multiple steps and extensive labor. These traditional methods also tend to generate significant waste and can be less environmentally friendly due to the use of cutting fluids and abrasives. As industries strive for sustainability and cost-effectiveness, there is a growing need for alternative finishing techniques that can deliver superior results with reduced environmental impact [6].

The Burnishing Process

Burnishing is an innovative surface finishing technique that has gained popularity for its ability to enhance surface quality without material removal. This chipless process involves the plastic deformation of the surface layer through the application of pressure, resulting in a smoother finish and increased hardness [7]. Unlike traditional machining methods, burnishing minimizes waste and can be performed in a single operation. One of the key advantages of burnishing is its ability to introduce compressive residual stresses in the material. These stresses can significantly improve the fatigue strength and wear resistance of components, making burnishing particularly beneficial for high-performance applications [8]. Additionally, the burnishing process can often be completed in less time than traditional methods, leading to increased productivity and cost savings.

Factors Influencing the Burnishing Process

Despite its advantages, the effectiveness of the burnishing process is highly dependent on several key parameters.

These include:

1. Spindle Speed: The rotational speed of the workpiece can significantly affect the burnishing action. Higher spindle speeds may enhance surface finish but can also lead to increased heat generation, which may negatively impact the material properties [3].
2. Feed Rate: The speed at which the burnishing tool moves across the workpiece influences the depth of plastic deformation. An optimal feed rate is necessary to achieve the desired surface quality without compromising the mechanical properties [9].
3. Burnishing Force: The amount of force applied during the burnishing process directly impacts the level of plastic deformation. Adequate force must be applied to induce the necessary surface changes while avoiding excessive material removal or damage [4].
4. Tool Material and Geometry: The material and design of the burnishing tool play a critical role in the process. Harder tool materials can withstand greater forces and pressures, while specific geometries can enhance the effectiveness of the burnishing action [9].
5. Lubrication: The use of lubricants during the burnishing process can reduce friction and heat

generation, leading to improved surface quality. Proper lubrication is essential for achieving optimal results [10].

Research Gap and Objectives

While burnishing has been applied to various materials, comprehensive studies focusing specifically on Aluminium Alloy 2024 and its unique properties are limited. Previous research has demonstrated the effectiveness of burnishing in improving surface quality and hardness in different alloys; however, the systematic optimization of burnishing parameters for 2024 aluminium remains an underexplored area [7].

This study aims to fill this gap by investigating the innovative application of burnishing to Aluminium Alloy 2024. We will systematically vary key parameters—spindle speed, feed rate, and burnishing force—using a specially designed roller-based tool mounted on a lathe machine. A full factorial design approach will enable us to assess the effects of these parameters on surface roughness and hardness comprehensively.

Methodology Overview

In this study, we employ advanced statistical analysis using Minitab software to evaluate the data collected from the burnishing experiments. This analysis will provide insights into the relationships between the burnishing parameters and the resulting surface characteristics. The use of regression methods will facilitate precise predictions of surface roughness and hardness based on the selected parameters.

Preliminary findings from our experiments indicate that optimal surface roughness (Ra = 0.05 μm) can be achieved under specific conditions—namely, a feed rate of 0.11 mm/rev, a spindle speed of 1000 r/min, and a burnishing force of 1000 N. These results highlight the potential of the burnishing process to enhance the mechanical properties of Aluminium Alloy 2024 significantly.

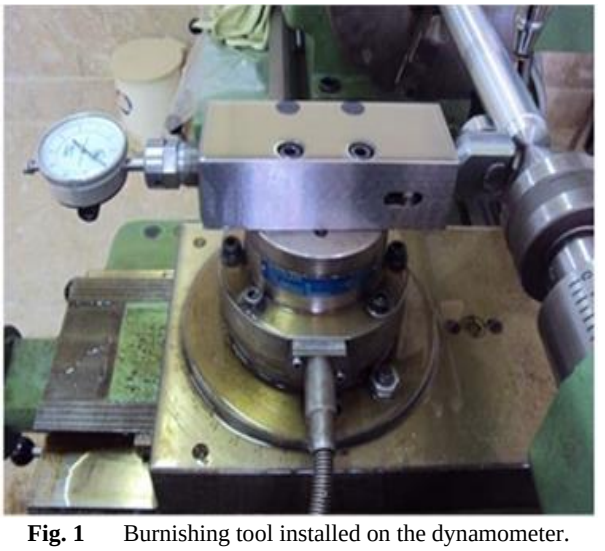

Fig. 1 Burnishing tool installed on the dynamometer.

Future Directions

The findings of this research not only validate the effectiveness of the burnishing process but also pave the way for improved industrial applications. Future studies will explore the effects of burnishing in corrosive environments and its impact on material strength, further expanding the applicability of this technique. Additionally, the investigation of alternative lubricants and tool materials may lead to further enhancements in the burnishing process. (“Fig. 1”).

2 METHODOLOGIES

The purpose of the current research is to design and build a burnishing tool to create the most desirable surface quality and hardness on non-metals that are not capable of creating a suitable surface quality (maximum Ra 1.0) with other machining operations. In addition to creating surface quality, such tools can cause surface hardness by creating compressive residual stress.

Devices and Tools

TN50BR model lathe is used to perform various burnishing operations. The control of deviations and slacks in the lathe should be done so that it does not exceed the limit value. It is clear that if the deviations and clearances of the machine tools are more than the specified limit, it will cause the failure or poor quality of the production part, and as a result, the results of the tests will be wrong. Allowed radial clearance in the lathe is 0.003 to 0.005mm. Axial clearance is taken by angular contact bearings. These bearings restrain the axial force in two directions and also bear the radial force behind the spindle. Roughness Tester, model RT-620 is a portable device used to measure the roughness of machined surfaces. A portable hardness tester based on the LEEB method has been used to measure hardness.

A special roller-based burnishing tool is used (“Fig. 2”). The set of experiments was carried out by this designed and built tool. This tool is used for burnishing on external surfaces with a round cross-section. The burnishing tool roll (7) can be replaced and can be made with different dimensions and materials. After being placed on the work piece, this roll is rotated by two support rollers (10) and performs the burnishing operation. In addition to the dynamometer, the burnishing force can be determined by the displacement of the spring, which is measured by the indicator clock. The base of this burnishing tool is closed by four screws on the dynamometer of the lathe. The dynamometer is used to measure the forces on the tool, which is developed based on piezo technology and is installed under the burnishing tool.

Aluminium is one of the light metals with a density of 2.7. Its corrosion resistance is excellent due to the existence of a sticky and stable layer of Aluminium

oxide on its surface. In other words, this oxide layer, whose thickness is about 0.025 microns, protects Aluminium against most corrosive substances. 2024 Aluminium alloy is used for making parts such as the fuselage and wings of airplanes due to its special properties such as special strength, high toughness, corrosion resistance, and good fatigue [10].

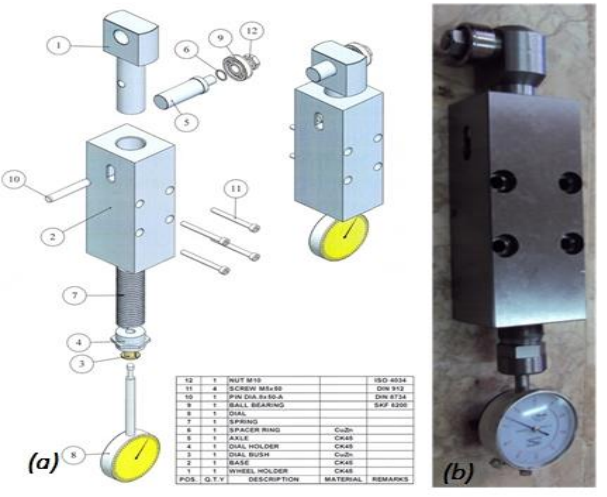

Fig. 2 Roller Burnishing Tool: (a): designed using CAD software, and (b): prototype.

The originality of Aluminium alloy 2024 including chemical composition, mechanical properties, and physical properties must be obtained from the seller or experimental tests.

Experiment Design

Many factors influence the output of this process, but the most significant parameters affecting the response variables in this research are:

Burnishing Rotation Speed: The number of rotations of the workpiece, measured in revolutions per minute (rpm).

Burnishing Advance: The feed rate of the burnishing tool for each revolution of the workpiece, measured in (mm/rev).

Burnishing Force: The force applied by the tool to the workpiece, measured in newtons. Alternatively, the depth of cut can be used as a substitute for burnishing force, measured in millimeters.

Each factor is tested at three different levels. "Table 1" presents the levels for each parameter, including spindle speed, feed rate, and burnishing force.

Table 1 The number of levels that can be obtained by each factor and its values in the burnishing test

N.	1	2	3	4	5	6	7	8	9
test	a1b1c1	a1b1c2	a1b1c3	a1b2c1	a1b2c2	a1b2c3	a1b3c1	a1b3c2	a1b3c3
N.	10	11	12	13	14	15	16	17	18
test	a2b1c1	a2b1c2	a2b1c3	a2b2c3	a2b2c2	a2b2c3	a2b3c1	a2b3c2	a2b1c1
N.	19	20	21	22	23	24	25	26	27
test	a3b1c1	a3b1c2	a3b1c3	a3b2c1	a3b2c2	a3b2c3	a3b3c1	a3b3c2	a3b3c3

"Table 2" is actually the same test plan based on the full factorial method. In this plan, three main factors each with three constant values are entered into the experiment, and in total three to the power of three and equivalent to 27 experiments will be performed. Values of 355, 710, and 1000 are considered for spindle speed, values of 0.11, 0.2, and 0.4 for feed rate, and values of 300, 600, and 1000 for burnishing force.

Table 2 Experimental design utilizing the full factorial method

Input parameters to branching machining			
Set point	a1	a2	a3
Spindle speed (n,rpm)	355	710	1000
Set point	b1	b2	b3
Feed rate (F_f, mm/rev)	0.11	0.2	0.4
Set point	c1	c2	c3
Branching force (F,N)	300	600	1000

The prepared material is cut into five equal pieces, each measuring 210 mm. A center drill is then created at both ends of the pieces, which are subsequently closed and machined on the lathe, as shown in "Fig. 3". The cutting of the outer surface of the parts is only to the extent of whitening and 0.5 mm, and two steps are created on both sides of them to close inside the chuck.

At the end, the dynamometer is installed on the superset of the lathe, and the tool is closed by four screws. During the burnishing process, the forces and torques caused by the reaction of the tool and the workpiece are applied to the dynamometer and will cause the piezoelectric-quartz strain in the dynamometer and produce an electrical signal. This produced signal is fed and amplified by communication cables to a multi-channel amplifier, and it measures the values of different forces.

After the installation of tools and workpieces, the number of tests will be performed according to their parameters and levels, in 27 test modes and two repetitions. Then the roughness and hardness values are measured and recorded in "Table 3".

Table 3 Surface roughness and hardness values of aluminium alloy 2024 after burnishingSurface

N.	test	Ra	hardness	N.	test	Ra	hardness	N.	test	Ra	hardness
1	a1b1c1	0.1717	174	10	a2b1c1	0.1219	172	19	a3b1c1	0.1304	169
2	a1b1c2	0.1259	184	11	a2b1c2	0.0783	180	20	a3b1c2	0.0591	176
3	a1b1c3	0.0307	192	12	a2b1c3	0.0669	190	21	a3b1c3	0.0328	186
4	a1b2c1	0.1744	174	13	a2b2c3	0.1986	170	22	a3b2c1	0.1089	167
5	a1b2c2	0.1144	182	14	a2b2c2	0.1504	180	23	a3b2c2	0.0889	177
6	a1b2c3	0.0493	191	15	a2b2c3	0.0843	187	24	a3b2c3	0.0545	184
7	a1b3c1	0.1215	172	16	a2b3c1	0.2089	166.5	25	a3b3c1	0.0763	165
8	a1b3c2	0.1130	181	17	a2b3c2	0.1770	177.5	26	a3b3c2	0.0832	176
9	a1b3c3	0.0487	191	18	a2b1c1	0.1509	183.5	27	a3b3c3	0.0856	184

Minitab software is used to determine the effect of each parameter on surface roughness and hardness. It is also possible to extract the results from the effect of factors in the form of two effects. Finally, the regression equation in the roughness and hardness of the surface will be done to find the optimal state.

Fig. 3 Analog-to-digital dynamometer converter and display screen, with the workpiece secured in the device for the burnishing process.

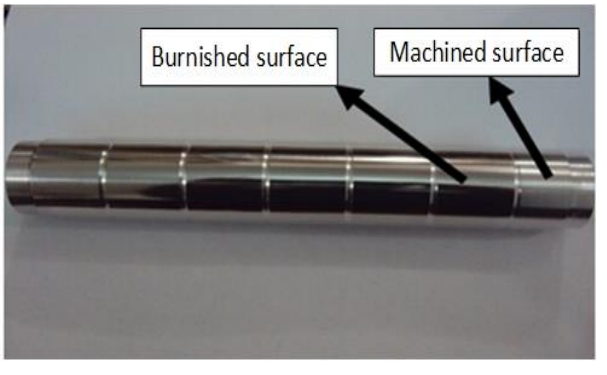

Fig. 4 Example of a burnished 2024 aluminium workpiece.

The primary workpiece has a roughness and hardness of 1.0846Ra and 164HV machined before the burnishing process. Figure 4 shows the machined workpiece surface and the burnished surface.

3 RESULTS

Burnishing of Aluminium 2024 was conducted using a lathe, and the resulting surface roughness and hardness values were obtained. This data was subsequently analyzed using Minitab software to complete the data processing. This processing includes the effect of the main factors and the effect of the two factors on the roughness and hardness of the surface. The graph related to them was extracted and the regression related to roughness and hardness was obtained according to the components including spindle speed, feed rate, and burnishing force.

The Effects of Main Factors on Surface Roughness

The separate effect of the three factors of spindle speed, feed rate and burnishing force by considering three separate values for each on the surface roughness of Aluminium 2024 was investigated (“Fig. 5”). The effect of spindle speed at speeds of 355, 710, and 1000 rpm on surface roughness was 0.137, 0.072, and 0.114 respectively. The second item is the feeding rate, which was obtained for 0.11, 0.20, and 0.40 surface roughness values of 0.100, 0.123, and 0.092, respectively. Finally, the effect of burnishing force with the values of 300, 600 and 1000N, the surface roughness was measured, and the values of 0.110, 0.096, and 0.119 were obtained, respectively. The amount of feed rate on surface roughness shows an increasing and then decreasing effect, while it shows the opposite effect for the two factors of spindle speed and burnishing force.

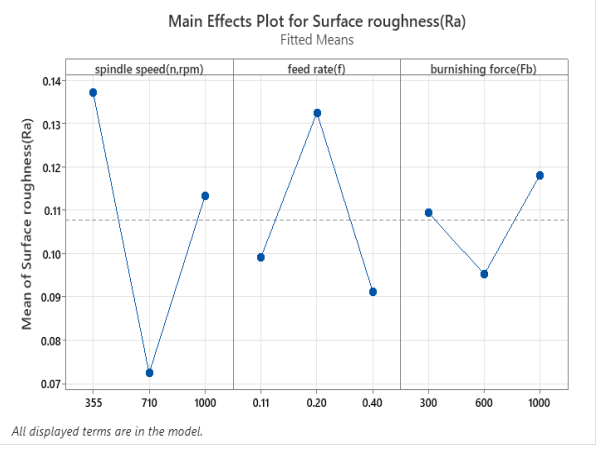

Fig. 5 Influence of Key Factors on Surface Roughness Resulting from Burnishing: (a): Spindle Speed, (b): Feed Rate, and (c): Burnishing Force.

The Effect of Two Factors on Surface Roughness

The effect of two factors on the surface roughness resulting from burnishing including spindle speed and feed rate, spindle speed and burnishing force, and feed rate and burnishing force is shown in "Fig. 6".

Spindle Speed and Feed Rate: Increasing the spindle speed from 355 to 710 and 1000 rpm yields the following surface roughness values: at a feed rate of 0.11 mm/rev, the values are 0.137, 0.088, and 0.072 µm; at a feed rate of 0.20 mm/rev, the values are 0.168, 0.068, and 0.165 µm; and at a feed rate of 0.40 mm/rev, the values are 0.107, 0.062, and 0.103 µm, respectively.

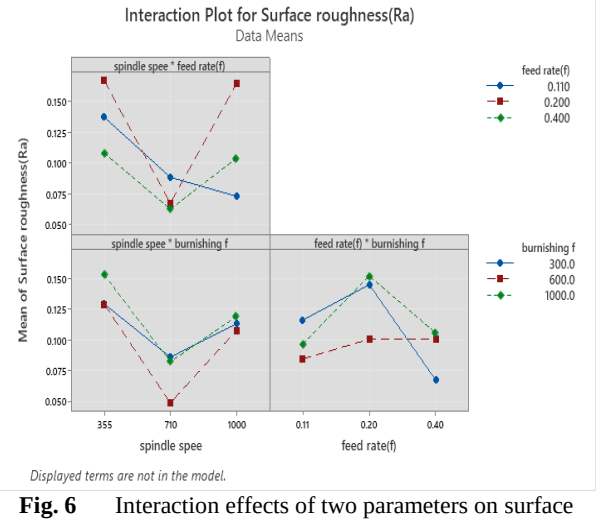

Fig. 6 Interaction effects of two parameters on surface roughness resulting from burnishing: (a): Spindle speed and feed rate, (b): Spindle speed and burnishing force, and (c): Feed rate and burnishing force.

Spindle speed and burnishing force: by increasing the spindle speed from 355 to 710 and 1000rpm, for the burnishing force 300N, the surface roughness value is 0.129, 0.088, and 0.114µm, for the burnishing force 600N, the surface roughness value is 0.130, 0.050 and 0.109µm, and for the burnishing force of 600N, the surface roughness values of 0.154, 0.084 and 0.120µm were obtained, respectively. A downward and upward trend was obtained for all three burnishing forces of 300, 600, and 1000N for surface roughness and with increasing spindle speed.

Feed Rate and Burnishing Force: As the feed rates increase to 0.11, 0.20, and 0.40 mm/rev, the following surface roughness values are observed: with a burnishing force of 300 N, the roughness values are 0.115, 0.148, and 0.069 µm; with a burnishing force of 600 N, the values are 0.087, 0.104, and 0.105 µm; and with a burnishing force of 1000 N, the roughness values are 0.100, 0.155, and 0.109 µm, respectively. In general, an upward and downward trend can be observed for the roughness surface value for three burnishing forces of 300, 600, and 1000N, and with an increase in the feed rate.

The Effects of Main Factors on Surface Hardness

The effect of three factors of spindle speed, feed rate, and burnishing force in different machining conditions was investigated separately on the surface hardness ("Fig. 7"). The results show that the spindle speed of 355, 710, and 1000 rpm causes the surface hardness to be 178.4, 181.6, and 176.9 in Vickers, respectively. With the feed rate of 0.11, 0.2, and 0.4, the surface hardness value is 174.8, 180.2, and 181.9 in Vickers respectively. By applying the burnishing force from 300 to 600 and finally 1000 N, the surface hardness was recorded as 178.3, 180.3, and 178.5, respectively. The feed rate has shown an increasing effect on the degree of hardness, while for the spindle speed and burnishing force, it reaches a maximum value from an initial value and then shows a decreasing effect.

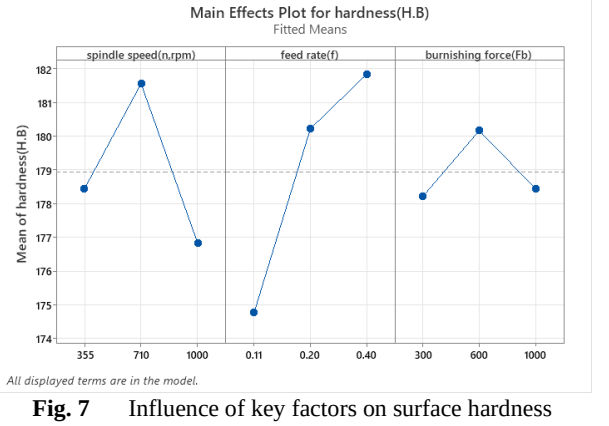

Fig. 7 Influence of key factors on surface hardness resulting from burnishing: (a): spindle speed, (b): feed rate, and (c): burnishing force

The Effect of Two Factors on Surface Roughness

The effect of two factors on the surface hardness resulting from burnishing including spindle speed and feed rate, spindle speed and burnishing force, and feed rate and burnishing force are shown in "Fig. 8".

Spindle speed and feeding rate: by increasing the spindle speed from 355 to 710 and 1000 rpm, with a feeding rate of 0.11mm/rev values of 176, 175 and 173HV, with a feeding rate of 0.20mm/rev values of 183, 183 and 174HV, with a feed rate of 0.40 mm/rev, values of 175, 186 and 184 HV are obtained, respectively, for the surface hardness. An upward and then downward trend can be seen for the feed rate of 0.200 and 0.400 mm/rev and only a downward trend for the feed rate of 0.11 mm/rev and with increasing spindle speed for the overall surface roughness.

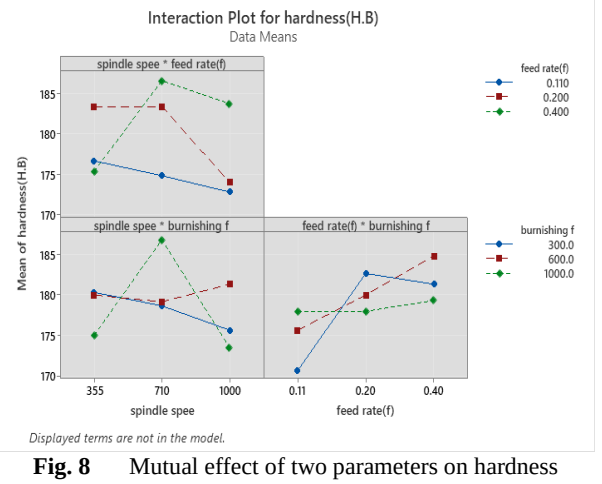

Fig. 8 Mutual effect of two parameters on hardness resulting from burnishing: (a): spindle speed and feed rate, (b): spindle speed and burnishing force, and (c): feed rate and burnishing force

Spindle speed and burnishing force: by increasing the spindle speed from 355 to 710 and 1000 rpm, for a burnishing force of 300N, surface hardness values are 180, 178, and 175HV, for a burnishing force of 600N, surface hardness values are 180, 178 and 181HV, and for the burnishing force of 600 N, surface hardness values of 174, 180 and 173HV were obtained, respectively. In total, a downward trend for the burnishing force of 300 N, a downward-upward trend for the burnishing force of 600N, and an upward-downward trend for the burnishing force of 1000N were obtained for surface hardness and with increasing spindle speed.

Feed Rate and Burnishing Force: As the feed rate increases to 0.11, 0.20, and 0.40 mm/rev, the surface hardness values are as follows: with a burnishing force of 300 N, the hardness values are 171, 183, and 181 HV; with a burnishing force of 600 N, the values are 176, 181, and 185 HV; and with a burnishing force of 1000 N, the values are 178, 178, and 179 HV, respectively. In general, an ascending-descending trend for hardness value for burnishing force 300N, an upward trend for hardness value for burnishing force 600N, and a downward trend for hardness value for burnishing force 1000N and with increasing feed rate mm/rev are visible.

Surface Roughness and Hardness Regression Equation and Model

The regression equation for surface roughness and hardness is given in equations 1 and 2, respectively. In these relationships, the effect of spindle speed, feed rate, and amount of burnishing force can be seen in the optimization.

Regression Equation for Surface roughness (Ra)= 0.10765+ 0.0294 spindle speed(n,rpm)_355 - 0.0352 spindle speed(n,rpm)_710 + 0.0058 spindle speed(n,rpm)_1000 - 0.0084 feed rate(f)_0.11 + 0.0249 feed rate(f)_0.20 - 0.0164 feed rate(f)_0.40 + 0.0019 burnishing force(Fb)_300 - 0.0124 burnishing force (Fb)_600 + 0.0105 burnishing force (Fb)_1000

(1)

Regression Equation for hardness (H.B)= 178.94 - 0.50 spindle speed(n,rpm)_355 + 2.61 spindle speed(n,rpm)_710 - 2.11 spindle speed(n,rpm)_1000 - 4.17 feed rate(f)_0.11+ 1.28 feed rate(f)_0.20 + 2.89 feed rate(f)_0.40 - 0.72 burnishing force(Fb)_300 + 1.22 burnishing force(Fb)_600 - 0.50 burnishing force (Fb)_1000 (2)

4 DISCUSSIONS

The current research focused on the burnishing process using a roller tool on Aluminium 2024, revealing critical insights into the parameters affecting surface roughness (Ra) and hardness. The findings underscore the significance of spindle speed and burnishing force while highlighting the relatively minor role of feed rate.

1. Influence of Power Parameters: The results indicate that spindle speed and burnishing force have a more pronounced effect on surface roughness than feed rate. Specifically, increasing spindle speed leads to a sharp decline in surface roughness values. For instance, at spindle speeds of 355, 710, and 1000 rpm, the surface roughness values were recorded as 0.137 µm, 0.072 µm, and 0.114 µm, respectively. This trend aligns with findings from previous studies, such as those by [7], who observed similar improvements in surface quality with increased spindle speeds in machining processes. This suggests a consensus in the literature regarding the effectiveness of higher spindle speeds in enhancing surface finish.

2. Surface Quality Improvements: The sharp decrease in surface roughness with increased spindle speed signifies the potential for achieving superior surface quality at elevated speeds. The optimal roughness achieved in this study (below 0.05 Ra) corroborates findings from [8], who reported comparable outcomes in their investigations of burnishing aluminum alloys. The improvement in surface finish can be attributed to

reduced contact time between the tool and the workpiece at higher speeds, which minimizes the adhesion and defect formation on the surface.

3. Minimal Effect of Feed Rate: An intriguing aspect of the results is the minimal impact of feed rate on surface roughness across all tested ranges (0.11, 0.20, and 0.40 mm/rev). While lower feed rates yielded marginally better roughness, this does not imply their practicality in operational settings. Studies by [5] have noted similar results, emphasizing that excessive reduction in feed rate can lead to increased contact time and, consequently, a rise in surface defects due to enhanced adhesion characteristics. Thus, while a minimum feed rate may optimize surface finish, it is essential to balance it with operational efficiency.

4. Production Efficiency: The findings suggest that burnishing can be effectively performed at high speeds without compromising surface quality. The negligible effect of feed rate allows for increased production speed, as operators can focus on optimizing spindle speed to achieve desired surface characteristics. This aspect resonates with the work of [3], who highlighted the economic benefits of burnishing in terms of time savings and reduced operational costs compared to traditional machining methods.

5. Comparative Analysis with Other Methods: When contrasted with conventional machining techniques, burnishing stands out as a superior method for achieving low surface roughness values. Traditional machining often results in higher roughness, particularly at increased feed rates. Additionally, previous research by [4] demonstrated that grinding methods are prone to rapid clogging, necessitating frequent re-sharpening. This not only increases costs but also results in inefficiencies that are not observed in the burnishing process.

6. Contributions to Existing Literature: This study contributes to the existing body of knowledge by providing a detailed analysis of the relationships between spindle speed, feed rate, and burnishing force, specifically for Aluminium 2024. The regression equations derived from the analysis offer a valuable framework for predicting surface roughness and hardness based on these parameters. This aligns with the findings of [7], who also utilized statistical modeling to optimize machining parameters in similar materials.

7. Conclusion on Burnishing: Overall, burnishing emerges as a highly effective method for enhancing the surface quality of Aluminium 2024. The process not only yields superior surface finishes but also proves to be economically viable, aligning with industrial demands for efficiency and quality.

Future studies will aim to explore the effects of burnishing on the mechanical strength of Aluminium 2024 in corrosive environments, as well as the impact of chemical surface corrosion. Investigating these aspects will provide deeper insights into the durability and long-term performance of burnished surfaces, further establishing the advantages of this technique in various operational contexts. By expanding the scope of research, we aim to contribute to the development of more robust manufacturing techniques that meet the evolving needs of the industry.

5 CONCLUSIONS

The burnishing process is influenced by several critical parameters, including burnishing force, feed rate, burnishing speed, lubrication type, tool material and diameter, the number of burnishing passes, and the initial surface roughness. This study specifically focused on analyzing how these factors affect the surface roughness and micro-hardness of Aluminium 2024.

The findings indicate that burnishing force and spindle speed have a more significant impact on surface roughness compared to feed rate. Notably, the optimal surface roughness, measured at less than 0.05 Ra, was achieved at the minimum feed rate in conjunction with maximum spindle speed and burnishing force. This highlights the importance of carefully balancing these parameters to enhance surface quality.

Additionally, the design of the rollers used in the burnishing tools allows for easy replacement and adjustment, contributing to prolonged tool life and simplified maintenance. The incorporation of lubrication in the form of an oil layer further reduces friction and heat generation during the process. This oil cooler creates a smooth working layer between the roller and the workpiece, effectively preventing material from adhering to the roller and enhancing overall burnishing performance.

These results provide valuable insights into the burnishing process, demonstrating that optimized control of force parameters and spindle speed can lead to significant improvements in surface roughness. This understanding is crucial for enhancing manufacturing processes that involve Aluminium 2024, especially in applications where surface quality is essential.

REFERENCES

[1] Thorat, S., Thakur, A., Optimization of Burnishing Parameters by Taguchi Based GRA Method of AA 6061 Aluminum Alloy, Materials Today: Proceedings, Vol. 5, No. 2, 2018, pp. 7394-7403.

[2] Samuel, A., et al. Effect of Machining of Aluminium Alloys with Emphasis on Aluminium 6061 Alloy–A Review, In IOP Conference Series: Materials Science and Engineering, IOP Publishing, 2021.

[3] Zhou, Z. Y., et al., Research on the Mechanism of The Two-Dimensional Ultrasonic Surface Burnishing Process to Enhance the Wear Resistance for Aluminum Alloy, Friction, Vol. 12, No. 3, 2024, pp. 490-509.

[4] Kumar, N., et al., Experimental Investigation of Effect of Roller Burnishing Process Parameters on Surface Roughness and Surface Hardness of C40E Steel, International Journal of Machining and Machinability of Materials, Vol. 18, No. 1-2, 2016, pp. 185-199.

[5] El-Tayeb, N., Low, K., and Brevern, P., Enhancement of Surface Quality and Tribological Properties Using Ball Burnishing Process, Machining Science and Technology, Vol. 12, No. 2, 2008, pp. 234-248.

[6] Raj, A., Chowdhury, A., and Ali, S. W., Green Chemistry: Its Opportunities and Challenges in Colouration and Chemical Finishing of Textiles, Sustainable Chemistry and Pharmacy, Vol. 27, 2022, pp. 100689.

[7] Raza, A., Kumar, S., A Critical Review of Tool Design in Burnishing Process, Tribology International, Vol. 174, 2022, pp. 107717.

[8] Amdouni, H., et al., Experimental Study of a Six New Ball-Burnishing Strategies Effects on The Al-Alloy Flat Surfaces Integrity Enhancement, The International Journal of Advanced Manufacturing Technology, Vol. 90, 201, pp. 2271-2282.

[9] Basak, H., Goktas, H. H., Burnishing Process on Al-Alloy and Optimization of Surface Roughness and Surface Hardness by Fuzzy Logic, Materials & Design, Vol. 30, No. 4, 2009, pp. 1275-1281.

[10] El-Tayeb, N., Low, K., and Brevern, p., Influence of Roller Burnishing Contact Width and Burnishing Orientation on Surface Quality and Tribological Behaviour of Aluminium 6061, Journal of Materials Processing Technology, Vol. 186, No. 1-3, 2007, pp. 272-278.

Int. J. Advanced Design and Manufacturing Technology, 2024, Vol. 17, No. 4, pp. 11-18

DOI: ***ISSN: 2252-0406*** ***https://admt.isfahan.iau.ir***

A Comparative FEM Analysis of a Substituted 3D-Printed U-Joint with PLA and ABS Materials

Mohammad Sajjad Mahdieh *
Department of Mechanical Engineering,
Shahid Chamran University of Ahvaz, Ahvaz, Iran
E-mail: s.mahdieh@scu.ac.ir
*Corresponding author

Golshid Fathinasab
Department of Mechanical Engineering,
Shahid Chamran University of Ahvaz, Ahvaz, Iran
E-mail: golshidfathinasab@yahoo.com

Received: 8 January 2024, Revised: 8 October 2024, Accepted: 2 November 2024

Abstract: Currently, manufacturing and repairing industrial equipment in a short time with the least cost has been a challenge. Furthermore, the idle time of the industrial machines due to their failed parts imposes high losses on the production process. Applying 3D printers to manufacture damaged parts quickly is a promising measure to tackle the abovementioned problem. This article is an efficient approach to the manufacture and analysis of a universal joint (U-joint) as the case study with Polylactic acid (PLA) and Acrylonitrile butadiene styrene (ABS) through the 3D printing process. U-joints are widely used as a coupling in industrial equipment to alleviate the misalignment of input and output shafts in many gearboxes and pumps. Because of undergoing fatigue loads, the failure occurrence in U-joints is very probable. Therefore, an attempt is made here to substitute this part with a 3D-printed one. Besides, comparing and evaluating the results of FEM simulations for the sake of selecting the most suitable material for the U-joint are done. According to the FEM results, the maximum stress imposed on the U-joint was obtained 28.8MPa which is lower than the yield strength of both PLA and ABS materials; however, the results show that PLA has higher fatigue strength than ABS in this case.

Keywords: ABS, 3D-Printing, FEM Analysis, Machine Components, PLA

Biographical notes: Mohammad Sajjad Mahdieh received his PhD in Mechanical Engineering from the University of Tehran, Iran. He is currently an Assistant Professor at the Department of Mechanical Engineering, Shahid Chamran University of Ahvaz, Iran. His research areas are inverse engineering, 3D printing, and metal forming. **Golshid Fathinasab** is a graduate of the Department of Mechanical Engineering, Shahid Chamran University of Ahvaz, Iran.

Research paper

1 INTRODUCTION

A universal joint is a connection between two shafts, typically yokes, that enables relative rotation around the y and z axes. This joint includes input and output shafts and an intermediate cross pin. Meaning that the input shaft is capable of transferring torque and rotary motion by means of cross to the output shaft. It is possible that rotation to be conveyed between the shafts while allowing misalignment in both axes. Car manufacturing, excavation, and robotics are examples of applications in which universal joints have been used. This explains why have been decided to consider it in a specific situation [1]. To manufacture most of the mechanical parts, applying finishing processes such as grinding, vibratory finishing, burnishing, and barrel finishing is inevitable [2-6]. Figure 1 shows the U-joint as the case study and its dimensions. 3D printing through quick and easy methods makes the production process more optimized and faster, thereby economizing on expenditures and time. Failing industrial parts not only causes excessive damage but also stops machines.

3D printers have solved these problems by constructing plastic components that have approximately similar properties to metal ones and can even temporarily work. There are some examples of profitable and practical consequences of using 3D printing. Cwekla et al. in 2017, studied mechanical strength properties of 3D-printed elements. Their research was carried out on a set of standardized samples, printed with low-cost standard materials (ABS), using a cheap 3D printer. The influence of parameters (such as the type of infill pattern, infill density, shell thickness, printing temperature, and the type of material) on selected mechanical properties of the samples, was tested [7].

In 2020, Kiendl et al. checked out the mechanical properties, especially toughness, strength, and stiffness, of FDM 3D-printed cases made of PLA. It was discovered that the material was isotropic in terms of stiffness and strength, but not at all in terms of toughness. furthermore, the material demonstrated much higher toughness when loaded cornerwise in comparison with loading parallel/perpendicular to the raster. It is possible to acquire optimized material performance purveying not only high strength but also high toughness simultaneously [8]. Goyanes et al. investigated the feasibility of using fused deposition modeling (FDM) with Hot Melt Extrusion (HME) and fluid bed coating to fabricate modified-release budesonide dosage forms [9]. Popa et al. in 2023, studied the experimental and numerical analyses of the impact parameters. They comprehended that materials made by additive manufacturing are able to be numerically modeled and calibrated with experimental ones. This means that the kinetic energies achieved in the numerical analysis of the PLA material had resemblance values to the experimental one [10]. FEM simulation helps to reduce the probable errors in manufacturing and the total cost [11-13].

Rarani et al. produced an industrial part with two different polymers: pure polylactic (PLA) and carbon fiber-reinforced PLA. Then they assessed the mechanical properties of the 3D printed samples through experiments such as tensile test and 3-point bending [14]. In addition, Akhoundi et al. investigated the effect of the filling pattern on tensile and flexural strength and modulus of the parts printed via fused deposition modeling (FDM), 3D printer [15]. Moreover, Vijayaraghavan et al. proposed an improved approach of multi-gene genetic programming (Im-MGGP) to formulate the functional relationship between wear strength and input process variables of the FDM process [16].

Deswal et al. in 2019, optimized significant process parameters including layer thickness, build orientation, infill density, and the number of contours for enhancing the magnitude/dimensional preciseness of fused deposition modeling (FDM) devise units [17]. San Andrés et al. probed about using 3D printing PLA and ABS materials for fine art. Samples were arranged in two diverse shapes (filament and printed parts). ABS showed noticeable changes against both sources of exposure (UV radiation and temperature), especially after UV aging, but PLA experienced more changes through temperature aging than UV radiation. This means that PLA generally demonstrated better stability than ABS [18].

In 2023, Karami Moghadam et al. studied how the CO2 laser cutting and Fused Filament Fabrication (FFF) 3D printing parameters influence the surface morphology of PLA samples. As a result of this article, through this way, not only the surface roughness of FFF parts was well diminished but also created a uniform surface texture [19]. In 2022, Martin et al. evaluated polymer composite based on PLA, elastomers, and cellulosic fibers through direct extrusion of crude materials in the pellet form for 3D printing. In general, these mentioned polymer composites were recognized as the most appropriate for pellet-based extrusion 3D printing [20]. It is worth mentioning that the 3D-printed parts may require machining processes to obtain the desired surface quality [21-27].

In this paper, a comparative analysis of a 3D-printed universal joint with PLA and ABS materials is accomplished. The industrial U-joint used as the case study in this project is shown in “Fig. 1”. This U-joint is applied to connect the small motor to the gearbox in a small drilling machine and this study attempts to substitute it with a 3D-printed one. Designing and simulation are done through SolidWorks software and Ansys Workbench software respectively. The most acceptable material of joint for use as a coupling in

industrial equipment in terms of life, safety factor, stress, and deformation should be concluded at the end. In addition, the U-joint is 3D printed by an FDM machine, and its function is investigated experimentally.

Fig. 1 Industrial U-joint as the case study.

2 MATERIALS AND METHODS

In this study, the feasibility of substituting a U-joint of an industrial machine's coupling with a plastic 3D-printed U-joint is investigated via FEM simulation. In this case, in order to calculate the functional life of the 3D-printed U-joint while applying in the coupling, the maximum bending stress, contact stress, and maximum strains are obtained through simulation by Ansys software. The specifications of the mentioned U-joint, the properties of the polymer used in the FDM machine, and the parameters adjusted in U-joint software are explained in the following.

2.1. Specifications of the U-Joint

In the first place, the universal joint was designed through SolidWorks software 2020. Designing includes two divisions, part, and assembly which are used for a 3D representation of a single design component and a 3D arrangement of parts or other assemblies respectively. Universal joints contain two driven yokes and a spider. In "Fig. 2" the 3D model of the U-joint performed in SolidWorks software is illustrated.

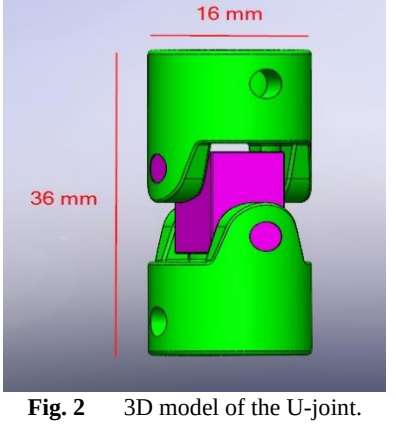

Fig. 2 3D model of the U-joint.

2.2. Properties of Materials and 3d Printing Machine

In this project, two polymers ABS and PLA which are very common for this purpose, are applied. The Mechanical properties of PLA and ABS filament used in the Property module of Ansys are presented in "Table 1".

Table 1 Mechanical properties of ABS and PLA

Properties	ABS	PLA
Elongation at Break	10 - 50 %	41.3 - 63.8%
Elongation at Yield	1.7 - 6 %	2.00%
Flexibility (Flexural Modulus)	1.6 - 2.4 GPa	3,280 MPa
Hardness Shore D	100	66
Stiffness (Flexural Modulus)	1.6 - 2.4 GPa	4.2 GPa
Strength at Break (Tensile)	29.8 - 43 MPa	38 - 47.8 MPa
Strength at Yield (Tensile)	29.6 - 48 MPa	37-46 MPa
Young Modulus	1.79 - 3.2 GPa	4.8 GPa

The model of the 3D printer applied in this present project is Ender-3 v2 neo of the Creality Company. The diameter of its nozzle is 0.4mm and the filament's feed rate is 50 mm/s. In addition, the diameter of the filament is 1.75mm. Figure 3 shows the 3D printer and filaments.

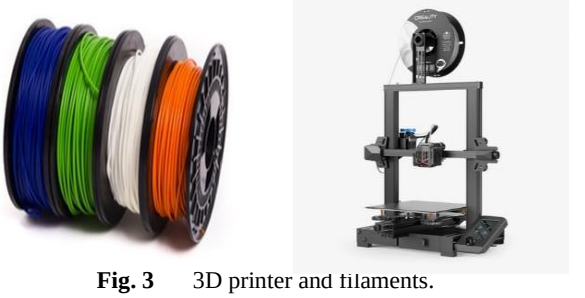

Fig. 3 3D printer and filaments.

Simulation Parameters

To analyze this problem in Ansys, three modules can be used: rigid dynamic, static structural, and transient structural. In the present study, the third module-transient structural- has been applied. The transient structural module is proper for problems with high deflection as well as high velocity. This module also has a higher analysis rate.

In the next step, connections among parts in the Connection module were defined. In the other world, the boundary conditions were set. In the Contact module, the action and reaction of parts when colliding with each other are defined. In this section, if no contact is defined between two parts, these two parts pass through each other. Therefore, three kinds of contacts can be defined among parts: frictional, sticking, and no frictional. In the

present project, the frictional contact was defined. Figure 4 shows the boundary conditions among parts. These constraints were defined as the movement and rotation of the U-joint being in harmony with the real one. The coefficient of friction was set equal to 0.2. The distributed torque was imposed to the one-half of the coupling equal to 1N.m. The value of this torque was obtained by calculating the output power of the gearbox and rotational speed.

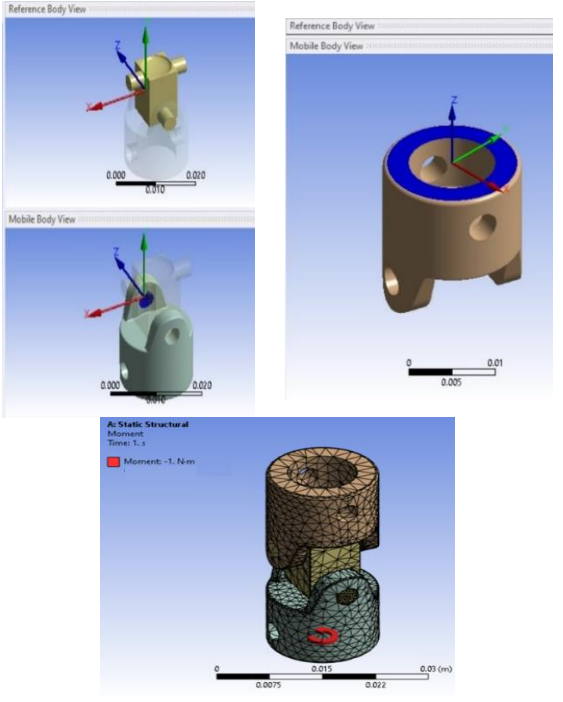

Fig. 4 Boundary conditions.

The Meshing is defined in the Mesh module. According to "Fig. 5", meshing was performed between the parts. Here, due to the significance of the pins of the connecting part and the holes of the coupling halves, these sections have fine mesh sizes; despite the other parts which have larger mesh sizes.

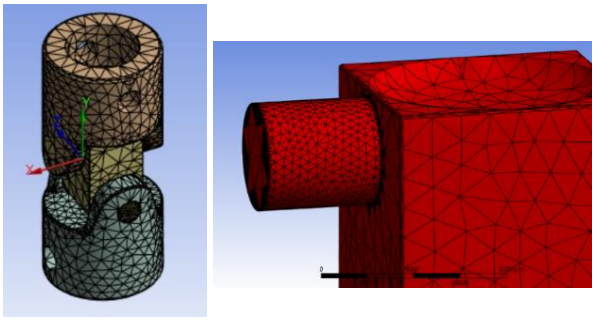

Fig. 5 Meshed parts.

If the mesh size of the whole of the mechanism is identical, the run time increases dramatically. The mesh size is 2mm and it is a 2D (surface mesh) type. In addition, the mesh control was applied to investigate the convergence of the results.

3 RESULTS AND DISCUSSIONS

In this entry, the feasibility of substituting a U-joint of an industrial machine's coupling with a plastic 3D-printed U-joint is investigated via FEM simulation. In this case, in order to calculate the functional life of the 3D-printed U-joint while applying the coupling, the maximum bending stress, contact stress, and maximum strains are obtained through FEM simulation by ANSYS software as follows.

3.1. Static Analysis

The first step involves evaluating the points that exhibit the highest stress levels. The values obtained for the stresses at these points must be compared to manually calculated results for validation purposes. By comparing these two sets of results and minimizing the error, the accuracy of the simulation is confirmed. Therefore, the most suitable material for constructing this universal joint can be determined by comparing the FEM results of two materials, ABS and PLA.

According to "Fig. 6", by imposing the torque to one-half of the coupling, the maximum stress was obtained and it is equal to 28.8MPa which is lower than the yield strength of both PLA and ABS materials. As it is obvious, the critical points are located at the spider part (on its pins). In reality, the same phenomenon occurs and most similar U-joints are damaged by their spiders.

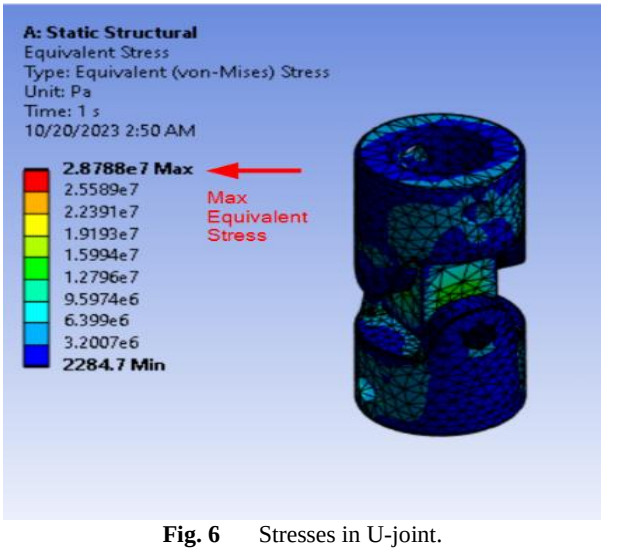

Fig. 6 Stresses in U-joint.

In this section, the manual analysis of the universal joint is presented. First, we manually calculated shear stress and bearing stress for the spider. Then, we identified the elements with the maximum stress values compared to

the calculated values. It was noteworthy that the obtained number for bearing stress is related to an element on the pin's surface, and the shear stress is calculated on the pin's cross-section. Finally, we determined the percentage of error between theoretical and software-generated values. The maximum bearing stress and shear stress on the spider's pin are manually calculated as follows.

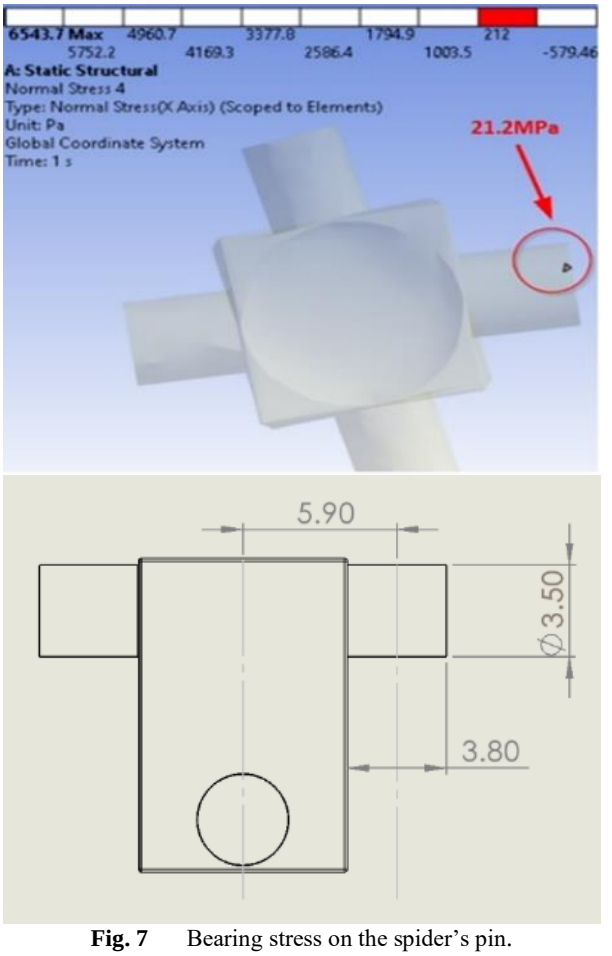

Fig. 7 Bearing stress on the spider's pin.

As following the equations, the bearing stress on the spider's pin was calculated at approximately 22.8 MPa. On the other hand, according to "Fig. 7", the maximum normal stress obtained by FEM analysis was 21.2MPa which indicates a 4.4% error.

$$T = 1NM$$

$$F = \frac{T}{2} \times r$$

$$\text{Bearing stress } \sigma = \frac{F}{A} = 22.8Mpa$$

$$\text{Error percentage: } \frac{22.8-21.2}{22.8} \times 100 \approx 4.42\%$$

The shear stress in the spider's pin has the same story. The manually calculated shear stress was equal to 20.9 MPa versus 21.2MPa obtained through FEM simulation ("Fig. 8") with a 1.5% error.

Then, to manually analyze the normal stress imposed on the corner of the half-coupling due to the bending phenomenon, this section was modeled with a cantilever beam as shown in "Fig. 9". Consequently, the maximum normal stress at the critical point was calculated at about 22.2MPa which is lower than the yield strength of the materials.

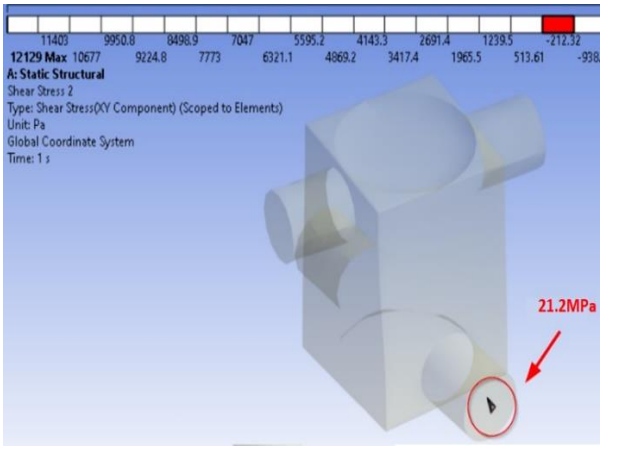

Fig. 8 Shear stress on the spider's pin.

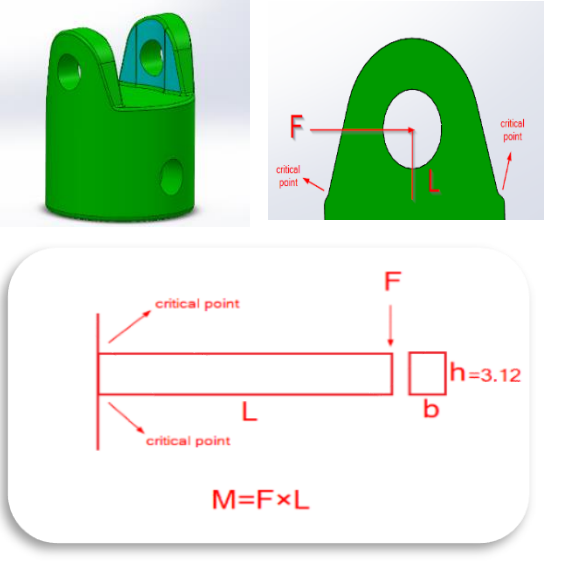

Fig. 9 Modelling of half-coupling with a cantilever beam.

3.2. Life Analysis

In this section, the lives of both materials (ABS & PLA) through fatigue analysis in static structural modules are determined and compared. The maximum stress is endured by spider. In fatigue analysis, where the piece gets damaged is investigated and the duration of this

process for both materials is obtained so that one can choose the best material for construction.
To calculate the life through the fatigue tool section, as shown in "Fig. 10", the loading type was supposed fully reversed with 1.1 as the scale factor and Soderberg as the mean stress theory.

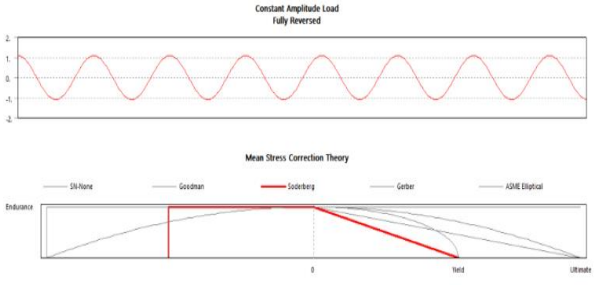

Fig. 10 Set parameters for life analysis.

Figure 11 shows the result of the life analysis for ABS material. As it is obvious, the critical elements (on the root of the spider's pin) endured about 2.67 million cycles. While, these elements in PLA material, endured 3.2 million cycles which indicates the higher fatigue strength of PLA.

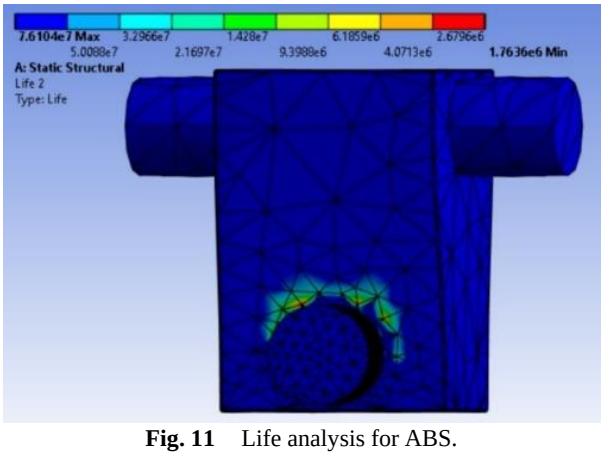

Fig. 11 Life analysis for ABS.

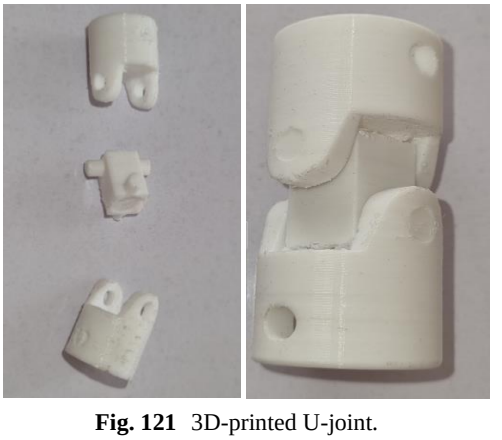

Fig. 121 3D-printed U-joint.

It is worth mentioning that the U-joint was manufactured through the 3D printer machine (demonstrated in "Fig. 12") and applied in the related mechanism. In addition, it has been working thoroughly and correctly without any failure within two months.

4 CONCLUSIONS

In this paper, a comparative analysis of a 3D-printed universal joint with PLA and ABS materials was accomplished. Designing and simulation were done through SolidWorks and Ansys Workbench software respectively. The FEM results were compared with analytical results, moreover, the endurance of the materials was investigated as well. The summary of the results is as follows:

- By imposing the torque to one-half of the coupling, the maximum stress was obtained 28.8MPa which is lower than the yield strength of both PLA and ABS materials.
- The bearing stress on the spider's pin was manually calculated at 22.8 MPa which has a 4.4% error with the FEM results.
- The manually calculated shear stress was equal to 20.9 MPa versus 21.2MPa obtained through FEM simulation with 1.5% error.
- The maximum normal stress at the critical point of the half-coupling was manually calculated at about 22.2MPa which is lower than the yield strength of the materials.
- The critical elements (on the root of the spider's pin) endured about 2.67 million cycles. While, these elements in PLA material, endured 3.2 million cycles which indicates the higher fatigue strength of PLA.

ACKNOWLEDGMENTS

We are grateful to the Research Council of Shahid Chamran University of Ahvaz for financial support (SCU.EM1403.39184).

REFERENCES

[1] Kohli, A., et al., Analysis of Universal Joint Using Virtual Simulation Method, Materials Today: Proceedings, Vol. 59, 2022, pp. 858-866.

[2] Mahdieh, M. S., Rafati, E., and Kargar Sichani, S., Investigation of Variance of Roller Burnishing Parameters on Surface Quality by Taguchi Approach. ADMT Journal, Vol. 6, No. 3, 2013.

[3] Saraeian, P., et al., Influence of Vibratory Finishing Process by Incorporating Abrasive Ceramics and Glassy Materials on Surface Roughness of CK45 Steel. ADMT Journal, Vol. 9, No. 4, 2016, pp. 1-6.

[4] Vakili Sohrforozani, A., et al., A Study of Abrasive Media Effect on Deburring in Barrel Finishing Process. Journal of Modern Processes in Manufacturing and Production, Vol. 8, No. 3, 2019, pp. 27-39.

[5] Vakili Sohrforozani, A., et al., Effects of Abrasive Media on Surface Roughness in Barrel Finishing Process. ADMT Journal, Vol. 13, No. 3, 2020, pp. 75-82.

[6] Mahdieh, M. S., Zadeh, H. M. B., and Reisabadi, A. Z., Improving Surface Roughness in Barrel Finishing Process Using Supervised Machine Learning, Journal of Simulation and Analysis of Novel Technologies in Mechanical Engineering, Vol. 15, No. 2, 2023, pp. 5-15.

[7] Ćwikła, G., et al. The Influence of Printing Parameters on Selected Mechanical Properties of FDM/FFF 3D-Printed Parts, In IOP Conference Series: Materials Science and Engineering, IOP Publishing, 2017.

[8] Kiendl, J., Gao, C., Controlling Toughness and Strength of FDM 3D-Printed PLA Components Through the Raster Layup, Composites Part B: Engineering, 2020, Vol. 180, pp. 107562.

[9] Goyanes, A., et al., Fabrication of Controlled-Release Budesonide Tablets via Desktop (FDM) 3D Printing, International Journal of Pharmaceutics, Vol. 496, No. 2, 2015, pp. 414-420.

[10] Popa, C. F., et al., Numerical and Experimental Study for FDM Printed Specimens from PLA under IZOD Impact Tests, Materials Today: Proceedings, Vol. 78, 2023, pp. 326-330.

[11] Mahdieh, M. S., Esteki, M. R., Feasibility Investigation of Hydroforming of Dental Drill Body by FEM Simulation. Journal of Modern Processes in Manufacturing and Production, Vol. 11, No. 2, 2022, pp. 71-83.

[12] Mahdieh, M. S., Monjezi, A., Investigation of an Innovative Cleaning Method for the Vertical Oil Storage Tank by FEM Simulation, Iranian Journal of Materials Forming, 2022.

[13] Mahdieh, M. S., et al., A Study on Stamping of Airliner's Tail Connector Part through FEM Simulation, Journal of Simulation and Analysis of Novel Technologies in Mechanical Engineering, 2023.

[14] Heidari-Rarani, M., Rafiee-Afarani, M., and Zahedi, A., Mechanical Characterization of FDM 3D Printing of Continuous Carbon Fiber Reinforced PLA Composites, Composites Part B: Engineering, Vol. 175, 2019, pp. 107147.

[15] Akhoundi, B., Behravesh, A. H., Effect of Filling Pattern on The Tensile and Flexural Mechanical Properties of FDM 3D Printed Products, Experimental Mechanics, Vol. 59, No. 6, 2019, pp. 883-897.

[16] Vijayaraghavan, V., et al., Process Characterisation of 3D-Printed FDM Components Using Improved Evolutionary Computational Approach, The International Journal of Advanced Manufacturing Technology, Vol. 78, No. 5, 2015, pp. 781-793.

[17] Deswal, S., Narang, R., and Chhabra, D., Modeling and Parametric Optimization of FDM 3D Printing Process Using Hybrid Techniques for Enhancing Dimensional Preciseness, International Journal on Interactive Design and Manufacturing (IJIDeM), Vol. 13, No. 3, 2019, pp. 1197-1214.

[18] San Andrés, M., et al., Use of 3D Printing PLA and ABS Materials for Fine Art, Analysis of Composition and Long-Term Behaviour of Raw Filament and Printed Parts, Journal of Cultural Heritage, Vol. 59, 2023, pp. 181-189.

[19] Karamimoghadam, M., et al., Influence of Post-Processing CO2 Laser Cutting and FFF 3D Printing Parameters on The Surface Morphology of PLAs: Statistical Modelling and RSM Optimisation, International Journal of Lightweight Materials and Manufacture, Vol. 6, No. 2, 2023, pp. 285-295.

[20] Martin, V., et al., Low-cost 3D Printing of Metals Using Filled Polymer Pellets, HardwareX, Vol. 11, 2022, pp. e00292.

[21] Mahdieh, M. S., The Surface Integrity of Ultra-Fine Grain Steel, Electrical Discharge Machined Using Iso-Pulse and Resistance–Capacitance-Type Generator. Proceedings of the Institution of Mechanical Engineers, Part L: Journal of Materials: Design and Applications, Vol. 234, No. 4, 2020, pp. 564-573.

[22] Mahdieh, M. S., Recast Layer and Heat-Affected Zone Structure of Ultra-Fined Grained Low-Carbon Steel Machined by Electrical Discharge Machining. Proceedings of the Institution of Mechanical Engineers, Part B: Journal of Engineering Manufacture, Vol. 234, No. 5, 2020, pp. 933-944.

[23] Mahdieh, M. S., Mahdavinejad, R., Comparative Study on Electrical Discharge Machining of Ultrafine-Grain Al, Cu, and Steel, Metallurgical and Materials Transactions A, Vol. 74, No. 12, 2016, pp. 6237-6247.

[24] Mahdieh, M. S., Zare-Reisabadi, S., Effects of Electro-Discharge Machining Process on Ultra-Fined Grain Copper, Proceedings of the Institution of Mechanical Engineers, Part C: Journal of Mechanical Engineering Science, Vol. 233, No. 15, 2019, pp. 5341-5349.

[25] Mahdieh, M. S., Mahdavinejad, R. A., A Study of Stored Energy in Ultra-Fined Grained Aluminum Machined by Electrical Discharge Machining. Proceedings of the Institution of Mechanical Engineers, Part C: Journal of Mechanical Engineering Science, Vol. 231, No. 23, 2017, pp. 4470-4478.

[26] Mahdieh, M. S., Mahdavinejad, R., Recast Layer and Micro-Cracks in Electrical Discharge Machining of Ultra-Fine-Grained Aluminum. Proceedings of the Institution of Mechanical Engineers, Part B: Journal of Engineering Manufacture, Vol. 232, No. 3, 2018, pp. 428-437.

[27] Mahdieh, M. S., Improving Surface Integrity of Electrical Discharge Machined Ultra-Fined Grain Al-2017 by Applying RC-Type Generator, Proceedings of

the Institution of Mechanical Engineers, Part E: Journal of Process Mechanical Engineering, 2023, pp. 09544089231202329.

Int. J. Advanced Design and Manufacturing Technology, 2024, Vol. 17, No. 4, pp. 19-27

DOI: ***ISSN: 2252-0406*** ***https://admt.isfahan.iau.ir***

Non-Linear Vibrations of Graphene Nanoplatelet-Reinforced Composite Beams using Non-Local Strain Gradient Theory

Ahmad Haghani*
Department of Mechanical Engineering,
Shahrekord branch, Islamic Azad University, Shahrekord, Iran
Energy and Environment Research Center,
Shahrekord branch, Islamic Azad University, Shahrekord, Iran
E-mail: a.haghani@iaushk.ac.ir, ahmad_h117@yahoo.co.uk
*Corresponding author

Received: 17 August 2024, Revised: 15 October 2024, Accepted: 2 November 2024

Abstract: With the growing integration of nanotechnology into everyday life and the importance of nanoelectromechanical systems, this article examines the non-linear free vibrations of an Euler-Bernoulli (EB) composite beam reinforced with graphene nanoplatelets (GN), considering the Non-Local Strain Gradient Theory (NLSGT). First, the elastic properties of the nanocomposite reinforced with GN were calculated using the rules of mixtures and the Halpin-Tsai (HT) model. Then, the Equations describing the motion for the EB beam were obtained through the virtual work law, the NLSGT, and the von Kármán (VK) strain field, and were analyzed through the homotopy technique. After solving the Equations, the obtained results were compared with those available in other sources, showing a very good agreement. Finally, the outcomes of varying the graphene plates (GPLs) weight fraction, the GPLs distribution, and the proportional ratio of length to thickness of the beam regarding the non-linear natural frequency (NF) were investigated where one of the important results of this paper is that the highest non-linear NF occurs first in the *X-GPLRC* distribution, then in the *A-GPLRC* distribution, and finally in the *O-GPLRC* distribution.

Keywords: Galerkin Method, GPLRC, Homotopy Analysis Method, Nonlocal Strain Gradient Theory (NLSGT)

Biographical notes: Ahmad Haghani received his PhD in Mechanical Engineering from the Science and Research Branch, Islamic Azad University, Tehran, Iran in 2017. He is currently an Assistant Professor at the Department of Mechanical Engineering, Shahrekord Branch, Islamic Azad University, Shahrekord, Iran. His current research interest includes FG-GPLRC and nonlocal strain gradient theory.

Research paper

1 INTRODUCTION

Nanoelectromechanical systems (NEMS) are considered one of the important branches of mechanical science, and beams are one of the critical components in NEMS, with widespread applications in nanocomposites. On the other hand, the classical theories in continuum mechanics have a limitation in studying the mechanical behaviour of nanostructures. These theories overlook the voids between atoms and the atomic forces within particles, which cannot be ignored in nanoscale problems. Therefore, considering the high cost of experimental studies at the nanoscale, generalized continuum mechanics theories have been proposed [1]. One such theory based on generalized continuum mechanics is the NLSGT [1-2]. Several studies have utilized this theory to solve various problems, including the following examples.

Yin and colleagues [3] investigated the vibrational behaviour of a curved nanotube subjected to supersonic airflow and internal fluid flow. They used the NLSGT to model the size-affected nanotube and derived the motion Equations through the use of Hamilton's principle (HP). To solve the Equations, the generalized differential quadrature technique was utilized.

Guo and colleagues [4] introduced a computational method to assess the non-linear electro-elastic wave scattering features in a nanoscale sandwich tube. They extracted the fundamental Equations of the problem by employing the NLSGT, HP, and the first-order shear deformation theory (FSDT). The Equations were then resolved through the finite element technique and neural networks to calculate the exact non-local functions and length scales under various conditions affecting the tube.

Biswas [5] investigated the distribution of harmonic plane waves in a non-local visco-thermo-elastic porous medium according to the NLSGT. The governing Equations were derived via the Green-Naghdi Type III model assumptions and the NLSGT. Finally, the impacts of the nonlocality length factor, viscosity, and porosity on phase speeds, damping factors, and wave infiltration depth at different frequencies were studied.

Trabelssi and colleagues [6] studied wave distribution in an EB nanobeam using the NLSGT. They employed HP to derive the beam's motion Equations and investigated the effects of the non-local factor and strain gradient (SG) factor on wave distribution. Phung-Van and colleagues [7] investigated the mechanical behavior of an FG nanosheet by employing the NLSGT. The study indicated that the mechanisms influencing stiffness in the nanoplate can be controlled by optimizing the non-local and SG factors. Liu and colleagues [8] investigated the free vibrations of an aluminum plate considering the NLSGT and molecular dynamics (MD) modelings. They calibrated the size factors in the NLSGT using MD modelings.

Singh and colleagues [9] predicted the bending specifications of an EB beam using the Moore-Gibson-Thompson thermoelasticity model along with the NLSGT. After deriving the governing Equations, they employed the Laplace transform and the wavelet estimation techniques to resolve these Equations. Behar and colleagues [10] investigated and analyzed the stability and vibrations of a rotating smart nanotube under electrical loads. They derived the boundary conditions and governing Equations using the NLSGT, EB beam theory, and HP and solved them using the Galerkin technique. Finally, they examined the impacts of the length scale of the material, non-local factors, rotational speed, boundary conditions, and external voltage on the NF.

Merzouki and Houari [11] performed an in-depth investigation of thermal vibrations in FG nanobeams, taking into account the temperature-dependent characteristics of the material. They used an extended finite element method based on the NLSGT to solve the problem and investigated 3 thermal loading categories.

Guerroudj and colleagues [12] studied the free vibrations of an FG nanobeam. They extracted the motion Equations using the higher-order SDT and the NLSGT. They also evaluated simple boundary conditions for the beam and examined the effects of structural geometry, gradient parameter, and non-local factors on the frequency of oscillation. Using nanocomposites reinforced with GN can impart diverse properties to the mechanical behavior of nanoplates and nanobeams [13]. Some of the research that has utilized these materials in the mechanical structures of nanoplates and nanobeams includes the following:

Bahranifard and colleagues [14] studied the non-linear vibration features and reactions of sandwich beams with graphene-reinforced coating layers and a porous core under moving loads. They extracted the motion Equations based on the FSDT and resolved the issues by the Newmark and Newton-Raphson methods. They found that the softening effects due to porosity rely on the arrangement of their distribution.

Safaei and colleagues [15] examined the out-of-plane free vibrations and responses to moving loads of curved sandwich beams with graphene-reinforced coating layers and a porous core. They extracted the governing Equations based on the FSDT and HP, and resolved them by differential quadrature technique and Newmark's technique. Numerical results showed that adding a small quantity of GPLs to the coating layers and core significantly changes the fundamental NF and movement ranges subject to the moving loads.

Mirzaei [16] studied the vibrations of composite plates reinforced with GN. The elasticity modulus of the plate was achieved by the HT law. The Equations governing the system were derived from the FSDT and addressed through the Ritz technique.

Ghatreh Samani and colleagues [17] investigated the free vibrations of a sandwich plate with two coating layers reinforced with GPLs. The motion Equations were established through HP and solved using the Navier technique. They ultimately examined the effect of the graphene plate pattern and their weight ratio on the natural frequencies.

Considering the research conducted on beams reinforced with GN and the NLSGT, it is evident that very few studies have been done on the use of GN combined with the NLSGT. The present work investigates the non-linear vibrations of an EB beam reinforced with carbon nanoplatelets according to the NLSGT. Initially, using the virtual work theory, classical deformation theory, NLSGT, and the VK strain field, the non-linear Equations of motion for the nanotube are derived. These Equations are then solved using the Galerkin and homotopy techniques [1]. Finally, after validating the solution, results on the variations in NF with different GPL distribution patterns, proportional ratio of length to thickness, and SG and non-local factors will be presented.

2 NON-LOCAL STRAIN GRADIENT THEORY (NLSGT)

In NLSGT [18], both the non-local elastic stress and the SG stress are considered. Therefore, the overall stress is written as follows:

$$(1-(ea)^2\nabla^2)\sigma_{xx} = E(1-l_s^2\nabla^2)\varepsilon_{xx}, \quad \nabla = \frac{\partial}{\partial x} \quad (1)$$

In this relation, E is the elastic modulus, ea is the non-local factor, and l_s is the SG length.

3 SIZE-AFFECTED EQUATIONS OF MOTION FOR AN EB BEAM

Figure 1 shows an EB beam with thickness h, length L, and width b.

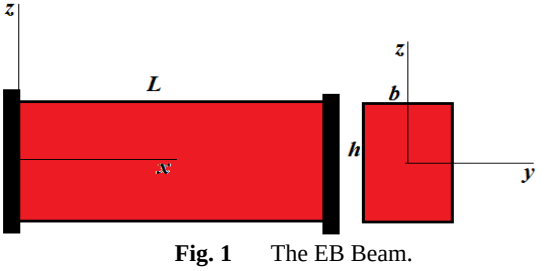

Fig. 1 The EB Beam.

The displacement field governing the EB beam is formulated as follows, where u_x is the movement along the direction of x, u_y is the movement along the direction of y, and u_z is the movement along the direction of z.

$$\begin{aligned} &u_x(x,z,t) = u(x,t) + z\frac{\partial w(x,t)}{\partial x}, \\ &u_y(x,z,t) = 0, \quad u_z(x,z,t) = w(x,t) \end{aligned} \quad (2)$$

Based on the VK strain theory and the movement field provided in "Eq. (2)", the non-linear strain field is calculated as follows.

$$\begin{aligned} &\varepsilon_{xx} = \frac{\partial u}{\partial x} + \frac{1}{2}\left(\frac{\partial w}{\partial x}\right)^2 - z\frac{\partial^2 w}{\partial x^2} \\ &\varepsilon_{xx}^{(1)} = \frac{\partial^2 u}{\partial x^2} + \frac{\partial w}{\partial x}\frac{\partial^2 w}{\partial x^2} - z\frac{\partial^3 w}{\partial x^3} \end{aligned} \quad (3)$$

To compute the motion Equations, the first-order variation of the strain energy δU, the first-order variation of the kinetic energy δK, and the first-order variation of the work done by external forces δW are first calculated. Then, using the calculus of variations and HP, the Equations of motion are derived.

The first-order variation of the strain energy δU is calculated according to the NLSGT using the subsequent Equation.

By substituting "Eq. (3) into Eq. (4)" and through the method of integration by parts, the subsequent Equation is obtained.

$$\begin{aligned} &\delta U = \int_V \left(\sigma_{xx} - \nabla\sigma_{xx}^{(1)}\right)\delta\varepsilon_{xx}dV + \int_A \sigma_{xx}^{(1)}\delta\varepsilon_{xx}dA \end{aligned} \quad (4)$$

By substituting "Eq. (3) into Eq. (4)" and using the method of integration by parts, the following Equation is obtained.

$$\begin{aligned} &\delta U = N\delta u\Big|_0^L + \left(N\frac{\partial w}{\partial x} + \frac{\partial M}{\partial x}\right)\delta w\Big|_0^L - M\delta\left(\frac{\partial w}{\partial x}\right)\Big|_0^L \\ &\quad - \int_0^L \left[\frac{\partial N}{\partial x}\delta u + \left(\frac{\partial}{\partial x}\left(N\frac{\partial w}{\partial x}\right) + \frac{\partial^2 M}{\partial x^2}\right)\delta w\right]dx \\ &\quad - M^{(1)}\delta\left(\frac{\partial^2 w}{\partial x^2}\right)\Big|_0^L + N^{(1)}\delta\left(\frac{\partial u}{\partial x} + \frac{1}{2}\left(\frac{\partial w}{\partial x}\right)^2\right)\Big|_0^L \end{aligned} \quad (5)$$

Where N is the resultant force and M is the resultant bending moment, and they are calculated according to the subsequent Equation.

$$\begin{aligned} &N^{(0)} = \int_A \sigma_{xx}dA, \quad N^{(1)} = \frac{\partial}{\partial x}\int_A \sigma_{xx}^{(1)}dA \\ &N = N^{(0)} - \frac{\partial N^{(1)}}{\partial x} \end{aligned} \quad (6)$$

$$M^{(0)} = \int_A \sigma_{xx} z dA\,, \quad M^{(1)} = \frac{\partial}{\partial x}\int_A \sigma_{xx}^{(1)} z dA$$
$$M = M^{(0)} - \frac{\partial M^{(1)}}{\partial x} \tag{7}$$

The first-order variation of the kinetic energy δK is given by the subsequent Equation.

$$\delta K = \rho A \frac{\partial u}{\partial t}\delta u\Big|_0^L + \rho I \frac{\partial^2 w}{\partial x \partial t}\delta\left(\frac{\partial w}{\partial t}\right)\Big|_0^L + \left(\rho A \frac{\partial w}{\partial t} - \rho I \frac{\partial^3 w}{\partial x^2 \partial t}\right)\delta w\Big|_0^L - \int_0^L \left[\rho A \frac{\partial^2 u}{\partial t^2}\delta u - \left(\rho I \frac{\partial^4 w}{\partial x^2 \partial t^2} + \rho A \frac{\partial^2 w}{\partial t^2}\right)\delta w\right] dx \tag{8}$$

Where A is the area of cross-sectional and I is the moment of cross-section inertia. Additionally, the first-order variation of the work done by external forces is given by the subsequent Equation.

$$\delta W = \int_0^L q\delta w\, dx \tag{9}$$

To compute the motion Equations, HP is used, which is given by the subsequent Equation.

$$\int_{t_1}^{t_2} (\delta K - \delta U + \delta W)\, dt = 0 \tag{10}$$

Based on the above Equation and "Eqs. (6) and (7)", the boundary conditions and motion Equations, assuming zero external forces, are obtained in the following form.

$$\frac{\partial N}{\partial x} = \rho A \frac{\partial^2 u}{\partial t^2}$$
$$\frac{\partial}{\partial x}\left(N\frac{\partial w}{\partial x}\right) + \frac{\partial^2 M}{\partial x^2} = \rho A \frac{\partial^2 w}{\partial t^2} - \rho I \frac{\partial^4 w}{\partial x^2 \partial t^2}$$
$$(1-(ea)^2\nabla^2)N = A_{11} b(1-l_s^2\nabla^2)\left(\frac{\partial u}{\partial x} + \frac{1}{2}\left(\frac{\partial w}{\partial x}\right)^2\right)$$
$$(1-(ea)^2\nabla^2)M = -D_{11} b(1-l_s^2\nabla^2)\frac{\partial^2 w}{\partial x^2}$$
$$N\delta u|_0^L = 0, \quad M\delta\left(\frac{\partial w}{\partial x}\right)\Big|_0^L = 0, \quad \left(N\frac{\partial w}{\partial x} + \frac{\partial M}{\partial x}\right)\delta w\Big|_0^L = 0$$
$$N^{(1)}\delta\left(\frac{\partial u}{\partial x} + \frac{1}{2}\left(\frac{\partial w}{\partial x}\right)^2\right)\Big|_0^L = 0, \quad M^{(1)}\delta\left(\frac{\partial^2 w}{\partial x^2}\right)\Big|_0^L = 0 \tag{11}$$

In the above Equation, the stiffness coefficients A_{11} and D_{11} are calculated according to the subsequent Equation.

$$A_{11} = \sum_{i=1}^{n}\int_{h_{i-1}}^{h_i}\left(\frac{E^{(i)}}{1-(\nu^{(i)})^2}\right)dz\,, \quad D_{11} = \sum_{i=1}^{n}\int_{h_{i-1}}^{h_i}\left(\frac{E^{(i)}}{1-(\nu^{(i)})^2}\right)z^2\, dz \tag{12}$$

To obtain the differential conditions for dynamic equilibrium in terms of displacement, it is assumed that the in-plane inertia is negligible. Therefore, the first term in "Eq. (11)" can be ignored [19]. Given that the beam is clamped at both ends, the classical and higher-order boundary conditions are provided by the subsequent Equation.

$$\delta u|_0^L = 0, \quad \delta\left(\frac{\partial w}{\partial x}\right)\Big|_0^L = 0, \quad \delta w|_0^L = 0$$
$$N^{(1)}\Big|_0^L = 0, \quad M^{(1)}\Big|_0^L = 0 \tag{13}$$

Therefore, according to "Eqs. (11) and (13)", the resultant force N is calculated using the subsequent Equation.

$$N = \frac{bA_{11}}{2L}\int_0^L \left(\frac{\partial w}{\partial x}\right)^2 dx \tag{14}$$

Based on the above information, the second Equation of "Eq. (11)" is rewritten regarding the displacements as follows:

$$bD_{11}(1-l_s^2\nabla^2)\frac{\partial^4 w}{\partial x^4} - (1-(ea)^2\nabla^2)N\frac{\partial^2 w}{\partial x^2} = (1-(ea)^2\nabla^2)\left(\rho I\frac{\partial^4 w}{\partial x^2 \partial t^2} - \rho A\frac{\partial^2 w}{\partial t^2}\right) \tag{15}$$

To solve the above Equation, the function $w(x)$ is initially assumed as follows:

$$w(x,t) = \chi_m(x)\varphi_m(t) \tag{16}$$

Considering the beam's clamped ends, the function $\chi_m(x)$ is assumed as follows [19]:

$$\chi_m(x) = 1 - cos\left(\frac{2m\pi}{L}x\right) \tag{17}$$

"Eq. (16)" is substituted into "Eq. (15)", and after differentiating and using the Galerkin technique, the subsequent Equation is obtained.

$$\frac{d^2\varphi_m(t)}{dt^2} + \omega^2\left(\varphi_m(t) + \eta\left(\varphi_m(t)\right)^3\right) = 0 \tag{18}$$

$$a_1 = \int_0^L (1-(ea)^2\nabla^2)\left(\rho A\chi_m(x) - \rho I\frac{d^2\chi_m(x)}{dx^2}\right)\chi_m(x)dx \tag{19}$$

$$a_2 = \int_0^L bD_{11}(1-l_s^2\nabla^2)\frac{d^4\chi_m(x)}{dx^4}\chi_m(x)dx \tag{20}$$

$$a_3 = -\left(\frac{bA_{11}}{2L}\int_0^L \left(\frac{d\chi_m(x)}{dx}\right)^2 dx\right)\int_0^L (1 - (ea)^2\nabla^2)\frac{d^2\chi_m(x)}{dx^2}\chi_m(x)dx \quad (21)$$

$$\omega^2 = \frac{a_2}{a_1}, \quad \eta = \frac{a_3}{a_2} \quad (22)$$

"Eq. (18)" is the Duffing Differential Equation, and its general initial conditions are as follows. To find the solution to this Equation, the homotopy technique is applied.

$$\varphi_m(0) = W, \quad \left.\frac{d\varphi_m(t)}{dt}\right|_{t=0} = 0 \quad (23)$$

4 HOMOTOPY SOLUTION TECHNIQUE

The homotopy technique is considered one of the most efficient semi-analytical techniques for solving non-linear differential Equations, which has rapid and successful convergence. Generally, a non-linear differential Equation can be considered as shown below, where N is the non-linear operator, $g(x)$ is the unknown operation, and x is the independent variable [20].

$$N[g(x)] = 0 \quad (24)$$

The homotopy combination is generally expressed by the subsequent Equation [20].

$$H[\mu(x;q); g_0(x), H(x), h, q] = (1-q)\{L[\mu(x;q) - g_0(x)]\} - qhH(x)N[\mu(x;q)] \quad (25)$$

Where $g_0(x)$ is the primary guess function for $g(x)$, $H(x)$ is a non-zero supplementary function, h is a non-zero supplementary factor, and L is a linear differential operator. Additionally, by varying the factor q from zero to one, the solution transitions from the primary guess function to the exact solution. When the right side of "Eq. (25)" is set to zero, the zero-order deformation Equation is obtained [20].

$$(1-q)\{L[\mu(x;q) - g_0(x)]\} = qhH(x)N[\mu(x;q)] \quad (26)$$

In the above Equation, if the value of q is set to zero, $\mu(x;0)=g_0(x)$ is obtained. Since the auxiliary function and auxiliary factor are non-zero, when q equals one, $\mu(x;1)=g(x)$ is obtained. Additionally, the m-th derivative of $g(x)$ is calculated as follows [20]:

$$g_m(x) = \frac{1}{m!}\left.\frac{\partial^m \mu(x;q)}{\partial q^m}\right|_{q=0} \quad (27)$$

According to Taylor's theorem, the function $g(x)$ can be expanded as a series according to the subsequent Equation.

$$g(x) \approx \sum_{k=0}^{m} g_k(x) \quad (28)$$

Additionally, the governing Equation for $g_m(x)$ is expressed as follows:

$$L[g_m(x)] = \chi_m L[g_{m-1}(x)] + hH(x)R_m(\vec{g}_{m-1}(x), x) \quad (29)$$

In the above Equation, χ_m and R_m are calculated according to the subsequent Equations.

$$\chi_m = \begin{cases} 0 & m \le 1 \\ 1 & otherwise \end{cases} \quad (30)$$

$$R_m(g_{m-1}(x), x) = \frac{1}{(m-1)!}\left\{\frac{\partial^{m-1}}{\partial q^{m-1}} N\left[\sum_{n=0}^{+\infty} g_n(x)\, q^n\right]\right\}\Big|_{q=0} \quad (31)$$

Using this method, "Eq. (18)" with the initial conditions given by "Eq. (23)" is solved [19], and the non-linear NF is calculated as follows:

$$\widetilde{\omega}^2 = \omega^2 \frac{(141\eta^2 W^4 + 384\eta W^2 + 256)}{32^2(4+3\eta W^2)^3} \quad (32)$$

"Eq. (32)" is non-dimensionalized as follows:

$$\omega^* = \sqrt{\frac{\widetilde{\omega}^2 L^4 \rho A}{b D_{11}^{(m)}}}, \quad D_{11}^{(m)} = \frac{E_m h^3}{12} \quad (33)$$

5 MECHANICAL PROPERTIES OF GPLRCS

The beam's material properties are shown in "Table 1".

Table 1 The material properties [13]

Material properties	Epoxy	GPL
E (GPa)	3.0	1010
ρ (Kg/m^3)	1200	1062.5
ν	0.34	0.186

In the present work, 3 pattern categories for the graphene-reinforced composite beam are considered. The *X* and *O* patterns represent symmetric distributions of GPLs, while the *A* pattern represents an asymmetric distribution of GPLs in the composite beam. The arrangement of these patterns is outlined in "Fig. 2".

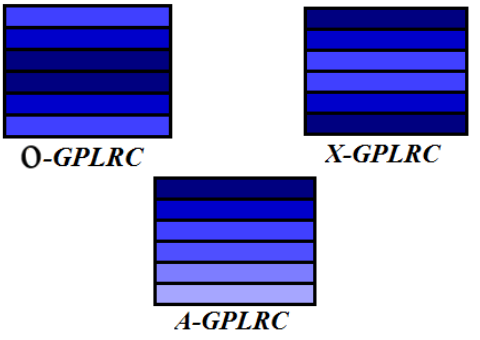

Fig. 2 Beam's GPL Distribution Patterns.

In this paper, it is assumed that N_L is an even number of layers of the graphene-reinforced composite. V_{GPL} is the GPLs volume fraction, which is computed for various patterns through the subsequent Equations [13].

$$X-GPLRC: V_{GPL}^{(i)} = 2\hat{V}_{GPL}\frac{|2i-N_L-1|}{N_L} \quad (34)$$

$$O-GPLRC: V_{GPL}^{(i)} = 2\hat{V}_{GPL}\left(1-\frac{|2i-N_L-1|}{N_L}\right) \quad (35)$$

$$A-GPLRC: V_{GPL}^{(i)} = \hat{V}_{GPL}\frac{|2i-1|}{N_L} \quad (36)$$

In these Equations, $V_{GPL}^{(i)}$ is the GPLs volume fraction for the *i*-th beam layer. $\hat{V}_{GPL}$ is the total GPLs volume fraction in the beam, and it is computed through the subsequent Equation, where W_{GPL} is the total GPLs weight fraction in the beam [13].

$$\hat{V}_{GPL} = \frac{W_{GPL}}{W_{GPL}+(1-W_{GPL})\left(\frac{\rho_{GPL}}{\rho_m}\right)} \quad (37)$$

To compute the effectiveness of each layer Young's modulus of the graphene-reinforced composite beam, the altered HT micromechanics framework is employed, which is expressed by the subsequent Equation [17].

$$E^{(i)} = \frac{3}{8}\left(\frac{1+\xi_L\eta_L V_{GPL}^{(i)}}{1-\eta_L V_{GPL}^{(i)}}\right)E_m + \frac{5}{8}\left(\frac{1+\xi_T\eta_T V_{GPL}^{(i)}}{1-\eta_T V_{GPL}^{(i)}}\right)E_m \quad (38)$$

$$\eta_L = \frac{\left(\frac{E_{GPL}}{E_m}\right)-1}{\left(\frac{E_{GPL}}{E_m}\right)+\xi_L}, \quad \eta_T = \frac{\left(\frac{E_{GPL}}{E_m}\right)-1}{\left(\frac{E_{GPL}}{E_m}\right)+\xi_T}$$

In the above Equation, ξ_L and ξ_T are the GPLs geometric factors, which are computed using the subsequent Equation. In this Equation, t_{GPL} b_{GPL}, and a_{GPL} are the thickness, width, and length of the GPL nanofillers, sequentially.

$$\xi_L = 2\left(\frac{a_{GPL}}{t_{GPL}}\right), \quad \xi_T = 2\left(\frac{b_{GPL}}{t_{GPL}}\right) \quad (39)$$

Based on the mixtures rule, for each layer of the graphene-reinforced composite beam, the density $\rho^{(i)}$ and Poisson's ratio $v^{(i)}$ are computed using the subsequent Equations. In these Equations, $V_m^{(i)} = 1 - V_{GPL}^{(i)}$ is the matrix volume fraction for every layer.

$$\rho^{(i)} = \rho_m V_m^{(i)} + \rho_{GPL} V_{GPL}^{(i)} \quad (40)$$

$$v^{(i)} = v_m V_m^{(i)} + v_{GPL} V_{GPL}^{(i)} \quad (41)$$

6 ASSESSMENT OF SOLUTION INDEPENDENCE WITH RESPECT TO THE NUMBER OF LAYERS

Figure 3 illustrates the alteration of the dimensionless non-linear NF ω^* with respect to the maximum non-dimensional transverse displacement $W^*=W/h$ for the case, where $\lambda_{NL}=ea/L=0.01<\lambda_{SG}=l_s/L=0.02$ and with an *X-GPLRC* distribution. Table (1) provides the mechanical specifications, with $L/h=20$ and the number of layers ranging from 6 to 14.

As can be seen from the graph, the curves for 10 to 14 layers converge, indicating that the solution becomes independent of the number of layers for 10 or more layers.

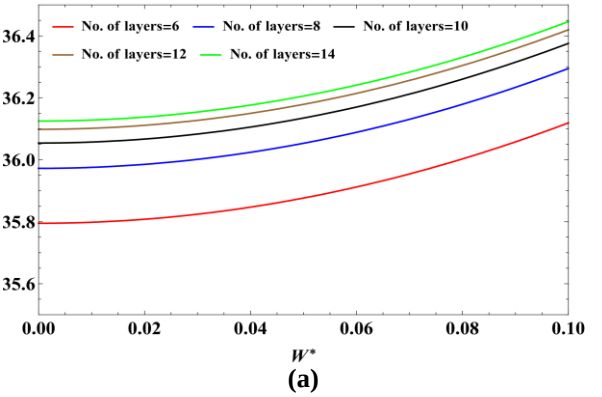

(a)

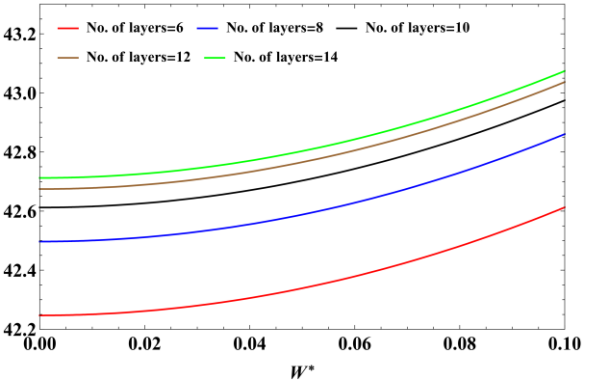

(b)

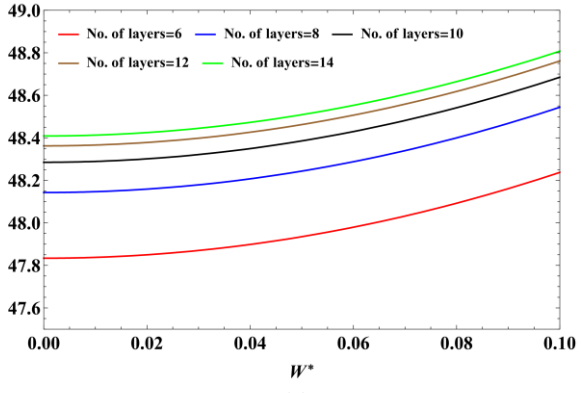

(c)

Fig. 3. Variation of the dimensionless non-linear NF regarding the maximum non-dimensional transverse displacement of the beam for (a) W_{GPL}=0.3%, (b) W_{GPL}=0.5%, and (c) W_{GPL}=0.7% for various numbers of layers.

7 SOLUTION VALIDATION

To validate the solution for an isotropic material, the results of the dimensionless non-linear NF ω^* regarding the maximum non-dimensional transverse displacement W^* are compared with the results of Faghidian [19] for two cases: λ_{NL}=0.01<λ_{SG}=0.02 and λ_{NL}=0.02>λ_{SG}=0.01, assuming L/h=20. The comparison shows very good agreement. Figure (4) illustrates the result of this comparison.

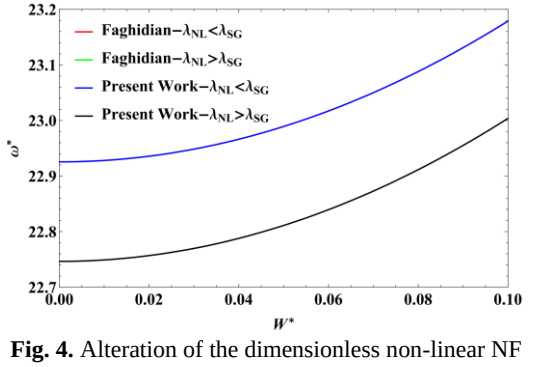

Fig. 4. Alteration of the dimensionless non-linear NF regarding the maximum non-dimensional transverse movement of the beam.

8 RESULTS AND DISCUSSION

In this section, the effects of variations in W_{GPL}, non-local factors, the SGT, and the ratio L/h on the dimensionless non-linear NF are examined. Table 1 provides the mechanical specifications considered for the present work. Figure 5 illustrates the impact of varying W_{GPL} on the dimensionless non-linear NF for *O-*, *X-*, and *A-GPLRC* distributions with L/h=20.

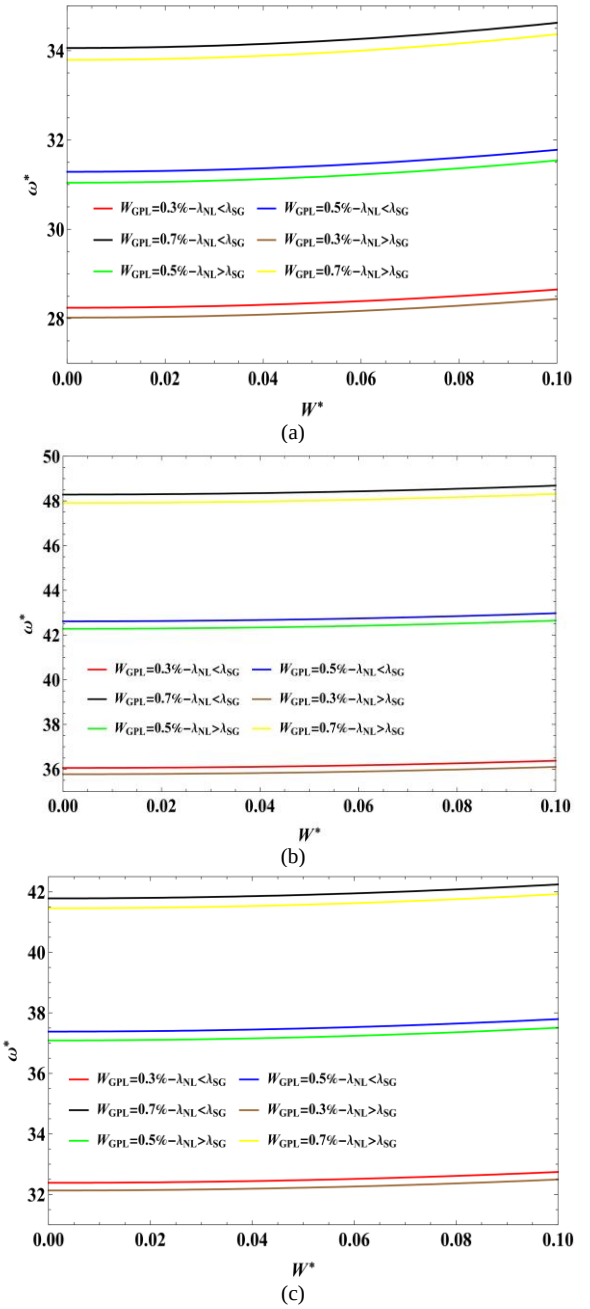

(a)

(b)

(c)

Fig. 5 Effect of varying W_{GPL} on the dimensionless non-linear NF for: (a): O-GPLRC, (b): X-GPLRC, and (c): A-GPLRC distributions.

As illustrated in the Figure, increasing W_{GPL} from 0.3% to 0.7% results in a rise in the NF. This can be attributed to the ibeam's enhanced rigidity as W_{GPL} increases for all three GPL distributions. Additionally, the NF is higher in the case where λ_{NL} =0.01<λ_{SG} =0.02 compared to when λ_{NL} =0.01>λ_{SG} =0.02. Moreover, the highest dimensionless non-linear NF occurs first in the *X-GPLRC* distribution, then in the *A-GPLRC* distribution, and finally in the *O-GPLRC* distribution. Figure 6 illustrates the effect of changing the L/h ratio on the

dimensionless non-linear NF for *O-GPLRC*, *X-GPLRC*, and *A-GPLRC* distributions, with W_{GPL} =0.5% and λ_{NL} =0.01<λ_{SG} =0.02. As seen from the figure, for all three distributions, *O-GPLRC*, *X-GPLRC*, and *A-GPLRC*, the dimensionless non-linear NF reduces with rising *L*/*h* ratio.

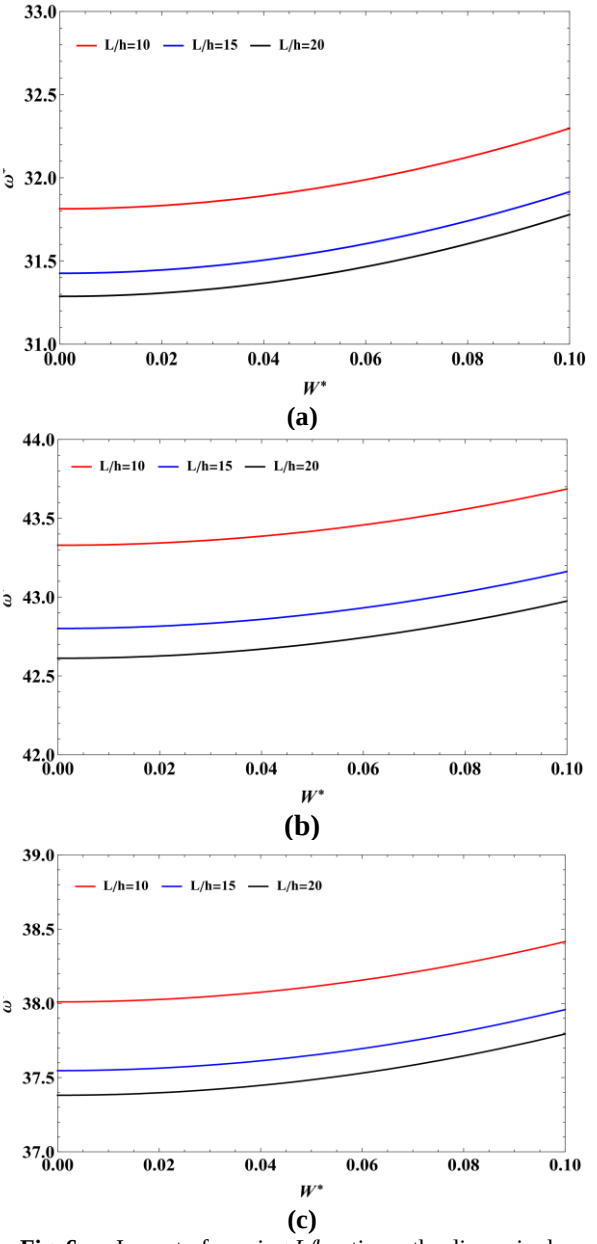

Fig. 6 Impact of varying *L*/*h* ratio on the dimensionless non-linear NF for: (a): O-GPLRC, (b): X-GPLRC, and (c): A-GPLRC distributions.

9 CONCLUSIONS

The present work investigates the non-linear free vibrations of EB beams reinforced with GN, considering the NLSGT. The elastic properties of the graphene nanoplatelet-reinforced nanocomposites were computed through the mixtures rule and the HT model. The governing Equations for the EB nanobeam were extracted through the virtual work law, NLSGT, and the VK strain field. Finally, the governing Equations were solved through the homotopy technique, and the impacts of varying GPL weight fraction, GPL distribution patterns, and the *L*/*h* ratio on the non-linear NF were examined. A summary of the findings is as follows:

- For all three GPL distributions, increasing W_{GPL} yields in rising in the non-linear NF. This results from the increased beam stiffness caused by the higher W_{GPL}.
- The NF is higher when $\lambda_{NL}<\lambda_{SG}$ compared to when $\lambda_{NL}>\lambda_{SG}$.
- The highest non-linear NF occurs first in the *X-GPLRC* distribution, then in the *A-GPLRC* distribution, and finally in the *O-GPLRC* distribution.
- In all three GPL distributions, the non-linear NF reduces with a rise in the *L*/*h* ratio.

10 NOMENCLATURE

Parameters	Definition
E	Elastic modulus
ρ	Density
ν	Poisson's ratio
ω^*	non-dimensional natural frequency
V	Volume fraction
W	Weight fraction
ea	non-local factor
l_s	SG length

REFERENCES

[1] Haghani, A., Jahangiri, M., and Ghaderi, R., Nonlinear Vibrations of Timoshenko Nanobeam Using Stress Driven Nonlocal Theory, Physica Scripta, Vol. 97, No. 7, 2022, pp. 095206.

[2] Zaera, R., Serrano, Ó., and Fernández-Sáez, J., On the Consistency of The Nonlocal Strain Gradient Elasticity, International Journal of Engineering Science, Vol. 138, 2019, pp. 65-81.

[3] Yin, J., Zou, Y., Li, J., Zhang, W., Li, X., and Habibi, M., Dynamic Stability and Frequency Responses of The Tilted Curved Nanopipes in A Supersonic Airflow via 2D Hybrid Nonlocal Strain Gradient Theory, Engineering Structures, Vol. 301, 2024, pp.117240.

[4] Guo, Y., Maalla, A., and Habibi, M., Electroelastic Wave Dispersion in The Rotary Piezoelectric NEMS Sensors/Actuators via Nonlocal Strain Gradient Theory,

Mechanical Systems and Signal Processing, Vol. 216, 2024, pp.111453.

[5] Biswas, S., The Propagation of Plane Waves in Nonlocal Visco-Thermoelastic Porous Medium Based on Nonlocal Strain Gradient Theory, Waves in Random and Complex Media, Vol. 34, No. 1, 2024, pp.372-403.

[6] Trabelssi, M., El-Borgi, S., and Friswell, M. I., Application of Nonlocal Strain Gradient Theory for The Analysis of Bandgap Formation in Metamaterial Nanobeams, Applied Mathematical Modelling, Vol. 127, 2024, pp. 281-296.

[7] Phung-Van, P., Hung, P. T., Nguyen-Xuan, H., and Thai, C. H., Small Scale Analysis of Porosity-Dependent Functionally Graded Triply Periodic Minimal Surface Nanoplates Using Nonlocal Strain Gradient Theory, Applied Mathematical Modelling, Vol. 127, 2024, pp. 439-453.

[8] Liu, C., Yu, J., Zhang, B., and Zhang, C., Size Parameter Calibration of Nonlocal Strain Gradient Theory Based on Molecular Dynamics Simulation of Guided Wave Propagation in Aluminum Plates, Thin-Walled Structures, Vol. 198, 2024, pp. 111659.

[9] Singh, B., Jangid, K., and Mukhopadhyay, S., Implementation of Legendre Wavelet Method for The Size Dependent Bending Analysis of Nano Beam Resonator Under Nonlocal Strain Gradient Theory, Computers & Mathematics with Applications, Vol. 153, 2024, pp. 94-107.

[10] Behar, M., Boukhalfa, A., and Aouinat, A. L., Examining the Critical Speed and Electro-Mechanical Vibration Response of a Spinning Smart Single-Walled Nanotube Via Nonlocal Strain Gradient Theory, Mechanics of Advanced Materials and Structures, 2024, pp. 1-17.

[11] Merzouki, T., Houari, M. S. A., Nonlocal Strain Gradient Theory for Free Vibration Analysis of FG Nano-scale Beams in Thermal Environments Using an Efficient Numerical Model, Journal of Vibration Engineering & Technologies, 2024, pp. 1-26.

[12] Guerroudj, M., Drai, A., Daikh, A. A., Houari, M. S. A., Aour, B., Eltaher, M. A., and Belarbi, M. O., Size-Dependent Free Vibration Analysis of Multidirectional Functionally Graded Nanobeams Via a Nonlocal Strain Gradient Theory, Journal of Engineering Mathematics, Vol. 146, No. 1, 2024, pp. 20.

[13] Haghani, A., Kiani, Y., Closed Form Expressions for Nonlinear Analysis of FG-GPLRC Beam Under Thermal Loading: Thermal Postbuckling and Nonlinear Bending, International Journal of Structural Stability and Dynamics, Vol. 24, No. 2, 2024, pp. 2450016.

[14] Bahranifard, F., Malekzadeh, P., and Golbahar Haghighi, M. R., Large Amplitude Vibration of Sandwich Beams with GPLRC Face Sheets and Porous Core Under Moving Load, Mechanics Based Design of Structures and Machines, Vol. 52, No. 3, 2024, pp. 1627-1650.

[15] Safaei, M., Malekzadeh, P., and Haghighi, M. G., Out-of-Plane Moving Load Response and Vibrational Behavior of Sandwich Curved Beams with GPLRC Face Sheets and Porous Core, Composite Structures, Vol. 327, 2024, pp. 117658.

[16] Mirzaei, M., Vibration Characteristics of Sandwich Plates with GPLRC Core and Piezoelectric Face Sheets with Various Electrical and Mechanical Boundary Conditions, Mechanics Based Design of Structures and Machines, Vol. 52, No. 2, 2024, pp. 990-1013.

[17] Ghatreh Samani, S., Beheshti, H., Akbarzadeh, A. H., and Kiani, Y., Frequency Assessment of Sandwich Rectangular Plates with an Anisogrid Core and GPLRC Face Sheets, International Journal of Structural Stability and Dynamics, 2024, pp. 2550175.

[18] Lim, C. W., Zhang, G., and Reddy, J., A Higher-Order Nonlocal Elasticity and Strain Gradient Theory and Its Applications in Wave Propagation, Journal of the Mechanics and Physics of Solids, Vol. 78, 2015, pp. 298-313.

[19] Faghidian, S. A., Reissner Stationary Variational Principle for Nonlocal Strain Gradient Theory of Elasticity, European Journal of Mechanics-A/Solids, Vol. 70, 2018, pp. 115-126.

[20] Liao, S., Advances in the Homotopy Analysis Method, World Scientific, China, 2013, pp. 1-35, 978-9814551243.

Int. J. Advanced Design and Manufacturing Technology, 2024, Vol. 17, No. 4, pp. 29-33

DOI: ***ISSN: 2252-0406*** ***https://admt.isfahan.iau.ir***

Application of the Homotopy Perturbation Method to Solve Nonlinear Equations Arising in Oscillatory Systems

Mohammad Javad Mahmoodabadi *, Neda Amiri
Department of Mechanical Engineering,
Sirjan University of Technology, Sirjan, Iran
E-mail: mohammadjavadmahmoodabadi@gmail.com,
nedaamiri1744@gmail.com
*Corresponding author

Received: 8 January 2024, Revised: 14 April 2024, Accepted: 30 July 2024

Abstract: In this research, the application of the homotopy perturbation method to solve nonlinear Equations arising in oscillatory systems is investigated. In this way, the performance of the Homotopy Perturbation Method (HPM) is compared with the numerical methods to find the solutions of nonlinear Equations in the vibration field. To this end, the Duffing–Holmes oscillatory model with nonlinear terms is regarded and solved by the HPM method. In order to validate the obtained solution by the HPM, the answers are compared with those of numerical methods. The results clearly depict that the homotopy perturbation method, without needing to small parameters, could present the answers near to the exact solutions and also to the numerical one.

Keywords: Duffing-Holmes Model, Homotopy Perturbation Method, Nonlinear Equations, Oscillatory Systems

Biographical notes: Mohammad Javad Mahmoodabadi received his BSc and MSc degrees in Mechanical Engineering from Shahid Bahonar University of Kerman, Iran in 2005 and 2007, respectively. He received his PhD degree in Mechanical Engineering from the University of Guilan, Rasht, Iran in 2012. During his research, he was a scholar visitor with Robotics and Mechatronics Group, University of Twente, Enchede, Netherlands for 6 months. Now, he is an Associate Professor of Mechanical Engineering at the Sirjan University of Technology, Sirjan, Iran. His research interests include optimization algorithms, nonlinear and robust control, robotics, and computational methods. **Neda Amiri** received her BSc in robotic engineering from the Sirjan University of Technology, Sirjan, Iran in 2020. Her current research focuses on robotic, and homotopy perturbation methods.

Research paper

1 INTRODUCTION

There are many engineering problems, such as those appearing in mechanical vibrations which are nonlinear, therefore most of them are solved by using numerical approaches, while the others are solved via the analytical methods. In the numerical methods, stability and convergence should be considered to avoid divergent or inappropriate results. On the other hand, many different analytical methods have been recently introduced to eliminate these issues. In this way, Kumar [1] presented a comprehensive literature review on the application of the Rayleigh-Ritz method to analyze vibration, static, and buckling characteristics of beams, shells, and plates by employing different theories. The governing Equations were obtained using the Rayleigh-Ritz method to study the effects of constituent volume fractions, slenderness ratios, and the beam theories on the natural frequencies by Pradhan and Chakraverty [2]. Yserentant [3] displayed some new error estimates for the eigenvalues and Eigen functions obtained by the Rayleigh-Ritz method, the common variational method to solve Eigen problems. Natural frequencies of rectangular plates were obtained by employing a set of beam characteristic orthogonal polynomials in the Rayleigh-Ritz method by Bhat [4].

A new implementation was developed by Lu et al. [5] based on a modified variational principle in which the Lagrange multipliers were replaced at the outset by their physical meaning so that the discrete Equations were banded. Thomas et al. [6] examined the conservation law structure of the continuous Galerkin method for solving the scalar, advection-diffusion Equation as a model problem. Demkowicz and Gopalakrishnan [7] discussed the principles and methodology of the discontinuous Petrov Galerkin method with optimal test functions and provided a literature review on the subject. Thomas et al. [8] developed a computational formulation that combines the advantages of discontinuous Galerkin methods with the data structure of their continuous Galerkin counterparts. Wazwaz [10] proposed a powerful modification of the Adomian decomposition method, introduced in the 1970s to the 1990s by George Adomian [9], to accelerate the rapid convergence of the series solution. Moreover, a simple method to determine the rate of convergence of the Adomian decomposition method was introduced by Hosseini et al. [11]. In this way, the application of the Adomian method for solving fuzzy systems of linear Equations was considered by Allahviranloo [12].

The solution of an initial value problem of the parabolic type was discussed by Tatari et al. [13] to propose an alternative method of solution, one not based on finite difference or finite element or spectral methods. The Kantorovich theorem, or Newton–Kantorovich theorem, as a mathematical statement on the semi-local convergence of Newton's method, was first stated by Leonid Kantorovich to form the Banach fixed-point theorem [14]. A Taylor–Galerkin method was described to derive finite element schemes for the scalar convection Equation in one or more space dimensions based on the forward-time Taylor series expansions by Donea [15]. Several explicit Taylor-Galerkin-based time integration schemes were proposed for the solution of both linear and non-linear convection problems with the divergence-free velocity by Timmermans et al. [16]. Shafiee Sarvestany and Mahmoodabadi [17] investigated a novel combination of the firefly optimization algorithm and artificial bee colony for mathematical test functions and real-world problems. Mahmoodabadi, and Nemati [18] presented an optimum numerical method for analysis of nonlinear conductive heat transfer problems. Mahmoodabadi and Sadeghi Googhari [19] studied numerical solutions of the time-dependent Schrodinger Equation by the combination of the finite difference method and particle swarm optimization.

In this research work, the basic idea of the HPM is introduced, its application on the oscillatory Equations is studied, and a comparison with the exact solution is also made.

2 HOMOTOPY PERTURBATION METHOD (HPM)

To illustrate the basic ideas of the HPM, the following nonlinear differential Equation is considered.

$$A(y) - f(\rho) = 0, \qquad \rho \in \Omega, \tag{1}$$

With boundary conditions:

$$B(y, \partial y/\partial n) = 0, \qquad \rho \in \Gamma, \tag{2}$$

Where A denotes a general differential operator, B represents a boundary operator, $f(\rho)$ signifies a known analytical function, and Γ is the boundary of domain Ω. Operator A can be generally divided into two linear (l) and nonlinear (N) parts. Therefore, "Eq. (1)" can be rewritten as follows:

$$L(y) + N(y) - f(\rho) = 0. \tag{3}$$

Hence, Homotopy function is constructed as follows:

$$H(\rho, v) = L(v) - L(y_0) + pL(y_0) + p[N(v) - f(\rho)] = 0, \tag{4}$$

Where ρ denoted the homotopy parameter.

According to the homotopy perturbation idea, the approximate solution of "Eq. (4)" can be expressed as a series of the powers of ρ, i.e:

$$y = \lim_{p\to 1} v = v_0 + v_1 + v_2 + \cdots, \quad (5)$$

3 APPLICATIONS OF THE HPM FOR DUFFING HOLMES OSCILLATOR

Consider the Duffing-Holmes oscillator Equation with the following state-space configuration:

$$\dot{y}_1(t) = y_2(t). \quad (6)$$

$$\dot{y}_2(t) = y_1(t) - 0.25y_2(t) - y_1^3 \quad (7)$$

By regarding:

$$y = y_1$$

And

$$\dot{y} = y_2$$

Then,

$$\ddot{y} + 0.25\dot{y} - y + y^3 = 0. \quad (8)$$

Therefore, the homotopy function is defined as follows:

$$H(p, v) = \ddot{v} + 0.25\dot{v} - v - L(y_0) + pL(y_0) + pv^3 = 0. \quad (9)$$

By employing $v = p^0v_0 + p^1v_1 + p^2v_2 + \cdots$, and boundary conditions $y(0) = 0.2$ and $\dot{y}(0) = 0.2$, the following relations are obtained:

$$H(p, v) = (p^0\ddot{v}_0 + p^1\ddot{v}_1 + p^2\ddot{v}_2 + \cdots) + 0.25(p^0\dot{v}_0 + p^1\dot{v}_1 + p^2\dot{v}_2 + \cdots) - (p^0v_0 + p^1v_1 + p^2v_2 + \cdots) + p^1[(p^0v_0 + p^1v_1 + p^2v_2 + \cdots)^3] = 0;$$
$$v_0(0) = 0.2, \quad \dot{v}_0(0) = 0.2, \quad (10)$$

By arranging the terms of the above Equation with respect to the power of parameter p, the following differential Equations are reached:

$$p^0: \ \ddot{v}_0 + 0.25\dot{v}_0 - v_0 = 0.$$
$$v_0(0) = 0.2, \quad \dot{v}_0(0) = 0.2. \quad (11)$$

$$p^1: \ \ddot{v}_1 + 0.25\dot{v}_1 - v_1 + (v_0)^3 = 0.$$
$$v_1(0) = 0, \quad \dot{v}_1(0) = 0. \quad (12)$$

$$p^2: \ \ddot{v}_2 + 0.25\dot{v}_2 - v_2 + (3{v_0}^2v_1) = 0. \quad v_2(0) = 0, \quad \dot{v}_2(0) = 0. \quad (13)$$

By utilizing the Laplace transformation on Equation (11), we have:

$$[s\hat{}2\, v_0(s) - sv_0(0) - v_0(0)] + 0.25[sv_0(s) - v_0(0)] - v_0(s) = 0. \quad (14)$$

Then,

$$V_0(s)(s^2 + 0.25s - 1) = 0. \quad (15)$$

Hence,

$$s_1 = 0.882, \quad s_2 = -1.132. \quad (16)$$

Therefore:

$$v_0 = \alpha e^{(-1.132t)} + \beta e^{(0.882t)},$$
$$v_0(0) = 0.2, \quad \dot{v}_0(0) = 0.2. \quad (17)$$

By employing the initial conditions, parameters α and β would be computed as follows:

$$\begin{cases} \alpha + \beta = 0.2 \\ -1.132\alpha + 0.882\beta = 0.2 \end{cases} \rightarrow \begin{cases} 1.132\alpha + 1.132\beta = 0.2264 \\ -1.132\alpha + 0.882\beta = 0.2 \end{cases} \quad (18)$$

By substituting $\alpha = -0.01$ and $\beta = 0.21$ for α and β into Equation (12), the first term of the solution could be introduced as follows:

$$v_0 = -0.01e^{(-1.132t)} + 0.21e^{(0.882t)}. \quad (19)$$

If Equation (12) is rewritten as follows:

$$v_1 = \ddot{v}_1 + 0.25\dot{v}_1 - v_1 + [(v_0)]^3. \quad (20)$$

If

$$[v_0]^3 = (-1 \times 10^{-6}e^{-3.396t}) + (0.0093e^{2.646t}) + (6.3 \times 10^{-5}e^{-1.382t}) + (-0.0013e^{0.628t}) \quad (21)$$

Then, particular solution z is formulated as follows:

$$z = a\, e^{-3.396t} + be^{2.646t} + ce^{-1.382t} + de^{0.632t} \quad (22)$$

With

$$\dot{z} = -3.396\, ae^{-3.396t} + 2.646\, be^{2.646t} - 1.382\, ce^{-1.382t} + 0.632\, de^{0.632t} \quad (23)$$

And

$$\ddot{z} = 11.5328\, ae^{-3.396t} + 7.0013\, be^{2.646t} + 1.9099\, ce^{-1.382t} + 0.3994\, de^{0.632t} \quad (24)$$

Therefore,

$$9.6828a + 6.6628b + 0.5644c - 0.4426d + [(-1 \times 10^{-6}e^{-3.396t}) + (0.0093e^{2.646t}) + (6.3 \times 10^{-5}e^{-1.382t}) + (-0.0013e^{0.628t})] = 0. \quad (25)$$

The following algebraic Equations will determine unknown parameters a, b, c, and d.

$$\begin{aligned} &9.6838a - 1 \times 10^{-6} = 0. \Rightarrow a = 1.0324 \times 10^{-7} \\ &6.6628b + 0.0093 = 0. \Rightarrow b = -0.0014 \\ &0.5644c + 6.3 \times 10^{-5} = 0. \Rightarrow c = -1.1162 \times 10^{-4} \\ &-0.4426d - 0.0013 = 0. \Rightarrow d = -0.0029 \end{aligned} \quad (26)$$

Finally, the particular solution is rewritten as follows.

$$z = 1.0324 \times 10^{-7}e^{-3.396t} - 0.0014e^{2.646t} - 1.1262 \times 10^{-4}e^{-1.382t} - 0.0029e^{0.628t} \quad (27)$$

By applying the general solution, the total relation for v_1 could be introduced as follows:

$$v_1 = \alpha e^{-1.132t} + \beta e^{0.882t} + (1.0327 \times 10^{-7}e^{-3.396t} - 0.0014e^{2.464t} - 1.1262 \times 10^{-4}e^{-1.382t} - 0.0029e^{0.628t} \quad (28)$$

Where, constant parameters α and β would be calculated by the following initial conditions:

$$v_1(0) = 0\,, \dot{v}_1 = 0. \quad (29)$$

$$v_1 = -0.0008\, e^{-1.132t} + 0.0058e^{0.882t} + 1.0327 \times 10^{-7}e^{-3.396t} - 0.0014e^{2.464t} - 1.1262 \times 10^{-4}e^{-1.382t} - 0.0029e^{0.628t} \quad (30)$$

Regarding the homotopy solution, the answer to the problem would be defined as follows:

$$y = \lim_{p \to 1} (\, v_0 + pv_1 + p^2v_2 + \cdots) \quad (31)$$

Finally,

$$y(t) = -0.01e^{(-1.132t)} + 0.21e^{(0.882t)} - 0.0008\, e^{-1.132t} + 0.0058e^{0.882t} + 1.0327 \times 10^{-7}e^{-3.396t} - 0.0014e^{2.464t} - 1.1262 \times 10^{-4}e^{-1.382t} - 0.0029e^{0.628t} \quad (32)$$

In order to validate the obtained solution by the HPM, the answers related to interval time [0, 10] (s) are compared with those of the fourth-order Runge-Kutta Method (RKM) in "Fig. 1". Although the results have a good agreement at the initial times, the differences could be obviously seen at the bigger times.

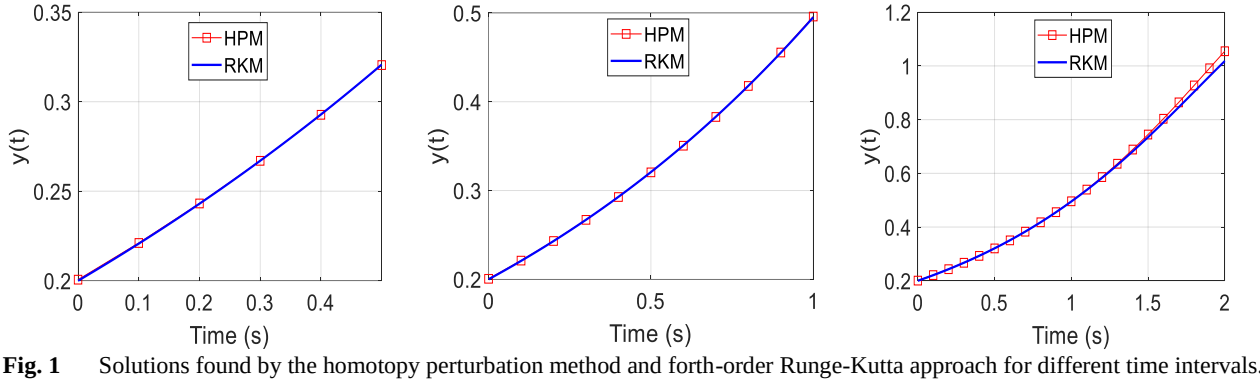

Fig. 1 Solutions found by the homotopy perturbation method and forth-order Runge-Kutta approach for different time intervals.

4 CONCLUSIONS

This research study implemented the homotopy perturbation method to analytically solve the nonlinear Dofing-Holmes Equation related to oscillatory dynamical systems. A closed mathematical formulation was determined to calculate the unknown parameter of the Equation at each time. The validations were performed through comparisons of the results with the numerical ones. The accuracy of the HPM was challenged by comparing the found results with those of the fourth-order Runge-Kutta technique.

REFERENCES

[1] Kumar, Y., The Rayleigh–Ritz Method for Linear Dynamic, Static and Buckling Behavior of Beams, Shells and Plates: A Literature Review, Journal of Vibration and Control, Vol. 24, No. 7, 2017.

[2] Pradhan, S., Chakraverty, K. K., Free Vibration of Euler and Timoshenko Functionally Graded Beams by Rayleigh–Ritz Method, Composites Part B: Engineering, Vol. 51, 2013, pp. 175-184.

[3] Yserentant, H., A Short Theory of the Rayleigh–Ritz Method, Computational Methods in Applied Mathematics, Vol. 13, No. 4, 2013, pp. 495–502.

[4] Bhat, R.B., Natural Frequencies of Rectangular Plates Using Characteristic Orthogonal Polynomials in Rayleigh-Ritz Method, Journal of Sound and Vibration, Vol. 102, No. 4, 1985, pp. 493-499.

[5] Lu, Y. Y., Belytschko, and T., Gu, L., A New Implementation of The Element Free Galerkin Method, Computer Methods in Applied Mechanics and Engineering, Vol. 113, No. (3–4), 1994, pp. 397-414.

[6] Thomas, J. R., Engel, H. G., Mats, L. M., and Larson, G., The Continuous Galerkin Method Is Locally Conservative, Journal of Computational Physics, Vol. 163, No. 2, 2000, pp. 467-488.

[7] Demkowicz, L. F., Gopalakrishnan, J., An Overview of the Discontinuous Petrov Galerkin Method, Recent Developments in Discontinuous Galerkin Finite Element Methods for Partial Differential Equations, Vol. 157, 2013, pp. 149–180.

[8] Thomas, J. R., Scovazzi Pavel, H. G., Bochev, B., and Buffa, A., A Multiscale Discontinuous Galerkin Method with The Computational Structure of a Continuous Galerkin Method, Computer Methods in Applied Mechanics and Engineering, Vol. 195, No. (19–22), 2006, pp. 2761-2787.

[9] Adomian, G., Solving Frontier Problems of Physics: The Decomposition Method, Kluwer Academic Publishers, 1994.

[10] Wazwaz, A. M., A Reliable Modification of Adomian Decomposition Method, Applied Mathematics and Computation, Vol. 102, No. 1, 1999, pp. 77-86.

[11] Hosseini, M. M., Nasabzade, H., On the Convergence of Adomian Decomposition Method, Applied Mathematics and Computation, Vol. 182, No. 1, 2006, pp. 536-543.

[12] Allahviranloo, T., The Adomian Decomposition Method for Fuzzy System of Linear Equations, Applied Mathematics and Computation, Vol. 163, No. 2, 2005, pp. 553-563.

[13] Tatari, M., Dehghan, M., and Razzaghi, M., Application of the Adomian Decomposition Method for the Fokker–Planck Equation, Mathematical and Computer Modelling, Vol. 45, No. (5–6), 2007, pp. 639-650.

[14] Ennis, J. E., The Kantorovich and Contractive Mapping Theorems, Numerical Methods for Unconstrained Optimization and Nonlinear Equations, 1983, pp. 92–94.

[15] Donea, J., A Taylor–Galerkin Method for Convective Transport Problems, International Journal for Numerical Methods in Fluids, Vol. 20, No. 1, 1984, pp. 101-119.

[16] Timmermans, L. J. P., Van De Vosse, F. N., and Minev, P. D., Taylor-Galerkin-Based Spectral Element Methods for Convection-Diffusion Problems, Namerical Methods in Fluids, Vol. 18, No. 9, 1994, pp. 853-870.

[17] Shafiee Sarvestany, A. R., Mahmoodabadi M. J., FA-ABC: A Novel Combination of Firefly Optimization Algorithm and Artificial Bee Colony for Mathematical Test Functions and Real-World Problems, Advanced Design and Manufacturing Technology, Vol. 15, No. 2, 2022, pp. 69-82.

[18] Mahmoodabadi, M. J., Nemati, A. R., A New Optimum Numerical Method for Analysis of Nonlinear Conductive Heat Transfer Problems, Journal of the Brazilian Society of Mechanical Sciences and Engineering, Vol. 43, 2021, pp. 1-8.

[19] Mahmoodabadi, M. J., Sadeghi Googhari F., Numerical Solution of Time-Dependent Schrodinger Equation by Combination of The Finite Difference Method and Particle Swarm Optimization, Journal of Research on Many-body Systems, Vol. 11, No. 1, 2021, pp. 114-127.

Int. J. Advanced Design and Manufacturing Technology, 2024, Vol. 17, No. 4, pp. 35-44

DOI: ***ISSN: 2252-0406*** ***https://admt.isfahan.iau.ir***

Algorithm Development and Design of Lattice Conical Shell Under Mechanical and Thermal Loads

Behrooz Shahriari *
Faculty of Mechanics, Malek Ashtar University of Technology, Iran
E-mail: shahriari@mut-es.ac.ir
*Corresponding author

Mahdi Sharifi
Faculty of Mechanics, Malek Ashtar University of Technology, Iran
E-mail: mahdisharifi13780@gmail.com

Hassan Izanlo
Faculty of Mechanics, Malek Ashtar University of Technology, Iran
E-mail: Hassanizanlo1998@gmail.com

Received: 30 January 2024, Revised: 12 June 2024, Accepted: 19 August 2024

Abstract: In this study, the development of a generative algorithm related to the lattice conical shell (Isogrid pattern) and the modeling of the stiffened shell under mechanical and thermal loads are discussed. An algorithm has been developed for the lattice conical shell (MATLAB software), which generates the pattern of stiffeners on the conical shell. Modeling of the lattice conical shell is done in SolidWorks software. The structure of stiffened shell is analyzed under loading using the Finite Element Method (FEM) in the ANSYS Workbench. The modeling of the lattice conical shell is investigated under mechanical (axial and bending load and internal pressure) and thermal loads. It is concluded that the stiffeners can resist buckling and mechanical failure under mechanical and thermal loading conditions, while the mass is significantly reduced. This shell can be used in various industries due to its lightweight and high resistance. Whereas the safety factor of the final model is about 2 and the model is acceptable for desirable internal pressure (0.6 MPa), the total system mass is about 41 kg.

Keywords: Design, Finite Element Method (FEM), Generative Algorithm, Lattice conical Shell

Biographical notes: Behrooz Shahriari was born in Isfahan, Iran in 1975. He received his BSc in Mechanical Engineering and MSc and PhD degrees in Aerospace Engineering from Malek Ashtar University of Technology in 2002, 2012, and 2016, respectively. His current research interests are structural optimization and artificial intelligence. **Mahdi Sharifi** received his MSc in Aerospace Engineering from the University of MUT, Isfahan, Iran, in 2024. His current research field is lattice conical shells. **Hassan Izanlo** is a researcher and his current research interests are optimization, robotic nonlinear dynamics, and nonlinear vibration.

Research paper

1 INTRODUCTION

In the aerospace industry, the efficiency of the structure is very important, which has made experts design these structures with high resistance and lightweight. Cone-shaped structures are structures that have many applications in various industries, including aerospace industries. The use of these shells in the aerospace industry is in the shells of engines, spaceship fuel tanks, etc. The lattice conical shell and Isogrid pattern are shells that have a special type of stiffener inside, outside or both. The mass of the thick shell structure is significantly decreased by redesigning it into a stiffened thin shell, while the reduction in strength is negligible. The stiffeners can have a rib and stringer combination in a simple form or a more complex form such as triangular, hexagonal, or square.

Kim [1] In his study, developed and tested stiffeners isogrid composite cylinder. He performed the axial compression test to extract the different failure modes in the structures such as the criticality of the ribs, shell buckling, and general instability. He proved that the isogrid cylinder can resist structural damage due to the large number of load paths; In this way, the cylinder continues to resist the compressive load even after breaking one or more ribs. In the experiment, it was determined that rib buckling is the critical failure mode for isogrid cylinders. Rahimi et al. [2] analyzed the buckling behavior of thin-walled GFRP cylindrical shells with triangular lattice stiffeners formed by helical and circumferential ribs under axial loading. They investigated different models of composite isogrid stiffener cylindrical shells with external diameter, shell thickness, height, and stiffeners that have the same properties, and constant cross-sectional area but different shapes and cross-sections. Their goal was to observe the effects of these differences on the buckling resistance of structures under axial load. They concluded that strengthening the shells increases the buckling load while decreasing the ratio of the buckling load to the weight of the unreinforced shell.

Totaro [3] analyzed the local buckling failure modes of triangular Latticed cylindrical shells in his study. He used accurate modeling to improve failure mode prediction. He verified the interaction of cross ribs and spiral ribs and investigated the effect of the number of shell sections, and the effect of pre-buckling tensile force on the ribs of the proposed model using finite element analysis. Eskandari Jam et al. [4] investigated the parameters affecting the design of anisogrid lattice conical shells and finally, they performed the buckling analysis of the lattice conical structure under axial loading, considering the relationships. Kim [5] made and tested the axial compression of reinforced composite isogrid panels. He performed this test to identify different failure modes in structures such as the critical condition of ribs, shell buckling, and general instability. He proved that the isogrid plate can resist structural damage due to a large number of load paths. Therefore, the plate resists the compressive load even after breaking one or more ribs. In the experiment, it was found that rib buckling is the critical failure mode for the isogrid plate. Sorrentino et al. [6] used coil robotics technology to fabricate an isogrid cylinder, made of composite materials. They performed geometric and structural tests on these structures and compared their results with the results obtained from hand-made structures. Their comparison determined the better quality of the robotic coil structures because these structures compiled with the geometrical changes and showed greater resistance to the axial compressive load.

Belardi et al. [7] presented a method for structural analysis and optimal design of composite anisogrid conical lattice structures subjected to various external loads. In this method, a finite element parametric modeling technique is used, which can manage all the geometrical parameters of the composite anisogrid lattice structure. Hao et al. [8] investigated the compression behavior of a natural fiber-based isogrid lattice cylinder made from pineapple leaf as fiber and phenol-formaldehyde resin as matrix, which is eco-friendly natural. They concluded that the lattice cylinder combined with the shell can be used to make a sandwich structure for use in parts of the building. Akl et al. [9] selected the best angle for the orientation of the stiffeners by presenting a logical design approach to optimize the static and dynamic characteristics of reinforced plates in the form of an isogrid.

Li et al. [10] designed an isogrid-shaped structure with T-shaped ribs to increase buckling resistance and plastic performance, manufactured it by 3D printing, and verified their model using finite element analysis. Totaro [11] formulated the constraint design Equations for longitudinally compressed lattice panels in buckling failure mode. His approach focuses on minimizing mass using analytic minimization. His approach was confirmed by the finite element results. Li and Fan [12] designed and manufactured a composite reinforced cylinder with carbon fiber in the form of an isogrid by applying the coiling and co-curing technique. They deduced the failure modes from the design of this optimized model in terms of minimum weight. Francisco et al. [13] optimized an isogrid structure considering six different responses using the sunflower algorithm to find the best shape. They optimized their model using multi-objective optimization. Pereira et al. [14] employed the multi-objective optimization of the isogrid pipe considering six objectives using the Lichtenberg algorithm to find the best design. In this regard, they used the finite element method to develop a numerical model for the complex structure.

The mentioned Studies did not consider the generative algorithm for modeling the lattice conical shell. They also did not consider the thermal conditions. In the current study, using the development of the generative algorithm for the lattice conical shell, generating and obtaining the angles and direction of the stiffeners on the conical shell will be developed. Then, using the angles and directions obtained for the stiffeners, the geometry of the lattice conical shell has been modeled in the SolidWorks software and analyzed for loading in the finite element software ANSYS Workbench under thermal and mechanical loads (compressive and axial). In order to validate the developed method, the Equations applied to the simple conical pressure vessel are derived. Finally, the results obtained from the finite element analysis are compared and validated with the numerical solution.

2 DEVELOPED ALGORITHMS

Generative algorithm development is a process that uses computational methods to achieve an optimizing algorithm that can optimize a set of data. In a generative algorithm development process, the required data and initial constraints are defined by the user, and the required outputs are requested from the algorithm. The algorithm developer must still use insight, knowledge, and intuition to develop the algorithm.

In this study, an algorithm is developed for the lattice conical shell that receives the large radius (R_1) and the small radius (R_2) of the incomplete cone. The inputs also contain the cone length (L) and initial stiffener angle. For this developed generative algorithm, a flowchart is presented that shows the implementation of this algorithm step by step ("Fig. 1").

The mentioned flowchart includes the steps that will display the required output. In order to specify the algorithm, the steps are explained:

Step 1- The large radius (R_1), the small radius (R_2) of the incomplete cone (a cone that has been cut on one or both sides), the length of the lattice conical shell (L), angle of the stiffeners (angle of stiffeners with flange) (β) and the spiral resolution (n=10000) are received from the user.

Step 2- Based on the received information, the conical shell is plotted as a three-dimensional diagram.

Step 3- The value of Z is specified using the linspace function, which creates a linearly spaced vector (equally spaced).

Step 4- The values of X and Y are determined according to the Equation governing the cone as well as the values of i and Z that have been selected in advance.

Step 5- The direction and angle of the first stiffener are determined and plotted in three dimensions by determining the values of X, Y, and Z.

Step 6 - The algorithm checks that if i=11, show the End, and if it is not, add one unit to it and return to step 4. The values of i must be less than or equal to 11. Choice 11 is to prevent stiffeners from overlapping each other.

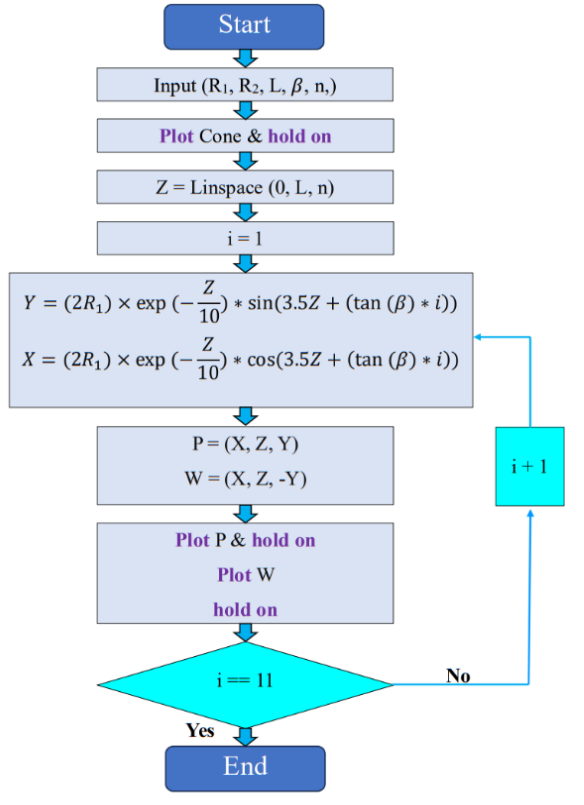

Fig. 1 Flowchart of the developed generative algorithm for lattice conical shell.

The algorithm used in this study is coded in MATLAB software ("Fig. 2").

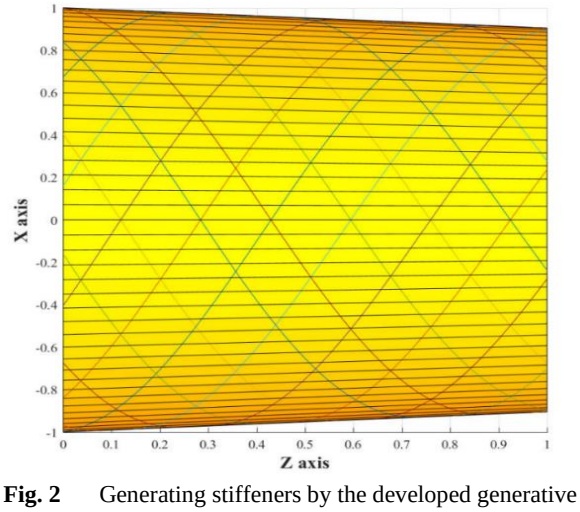

Fig. 2 Generating stiffeners by the developed generative algorithm for lattice conical shell.

3 MODELING

Whereas the modeling of the lattice conical shell is difficult due to its complex structure, the developed algorithm verified the mathematical model of the stiffener. Therefore, this pattern is designed in SolidWorks software as a three-dimensional model.

3.1. Introduction of The Structure

The lattice conical shell is an incomplete cone (a cone that has been cut on one or both sides). This shell has dimensional specifications and these values are presented in "Table 1" for the mentioned structure.

Table 1 Dimensional characteristics of lattice conical shell

Parameter	Value
Large radius (R_1)	0.5 m
Small radius (R_2)	0.446 m
Slope of the cone (θ)	3 deg
Length of the cone (L)	1 m

In this study, a lattice conical shell made of Inconel 718 material is designed. Inconel 718 is a nickel-chromium superalloy that has high strength and corrosion resistance and is used in the temperature range of -253 to 704 degrees Celsius. The hardness of the alloy increases through the aging process, and its production and shaping capabilities are also reachable. This alloy has good weldability and its resistance to cracking caused by stress is also very desirable. The presence of features such as ease and economy in manufacturing along with high tensile strength, desirable fatigue, creep behavior, and acceptable rupture strength have made Inconel 718 widely used in the industry. The mechanical and thermal properties of Inconel 718 are presented in "Table 2".

Table 2 Mechanical and thermal characteristics of Inconel 718 [15]

Properties	Value
Density	8170 ($^{kg}/_{m^3}$)
Ultimate tensile strength	1243 MPa
Yield tensile strength	1154 MPa
Modulus of elasticity	200 GPa
Elongation at the breaking	%18
thermal conductivity	11.4 w/m-k

3.2. Modeling Method

The modeling of the lattice conical shell with the mentioned dimensions has been done in the SolidWorks software. For the modeling method, a flowchart is developed that shows step-by-step modelling of the lattice conical shell ("Fig. 3").

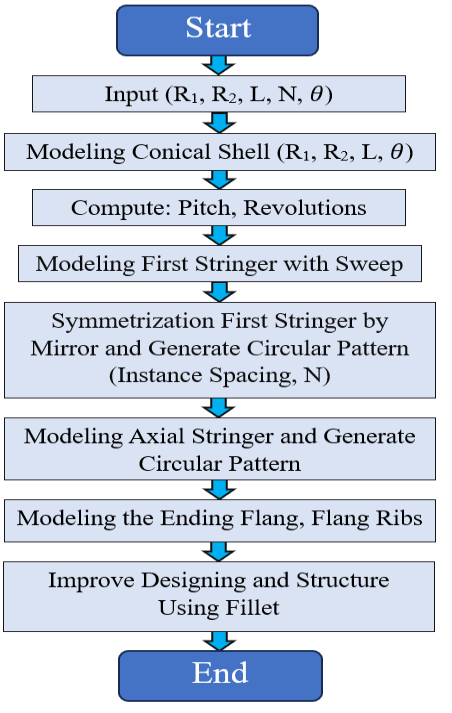

Fig. 3 Conical shell modeling flowchart.

The above flowchart contains steps that show how to model. The step-by-step explanation to clarify the details:

Step 1- To model the lattice conical shell, the geometry of the cone is generated with the large radius (R_1), the small radius (R_2), the slope of the cone (θ), and the length of the cone (L).

Step 2- To model stiffener, the results of the algorithm are used, and Revolution and Pitch are calculated. Then, the first stiffener is modeled by drawing the geometry of the cross-section and using the Sweep command.

Step 3- Another stiffener is modeled, by Symmetrization the first stiffener is in the opposite direction. The CirPattern command is used to generate stringers (N=24) on the lattice conical shell.

Step 4- To increase the strength and resistance to buckling, stiffeners are created horizontally (in line with the cone) and more are generated with the CirPattern command.

Step 5- Two flanges are modeled at the beginning and end of the shell so that it can be loaded. To prevent buckling near the flanges, two ribs are modeled which have the same height as the other stiffeners.

Step 6 - Fillets are used to reduce the stress concentration and distribute the stress more evenly between the lattice conical shell and the stiffeners.

The final geometry is prepared for finite element analysis ("Fig. 4").

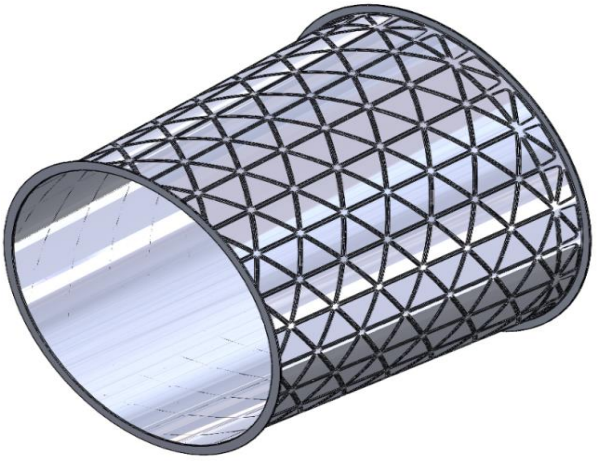

Fig. 4 Final model of lattice conical shell.

4 FINITE ELEMENT ANALYSIS

The lattice conical shell should be subjected to loading after modeling. The analysis of this shell has been done in the ANSYS finite element software of the Static Structural part. In this analysis, very fine shell meshing is considered to get the best result (“Fig. 5”). A tetrahedral element has been used for finite element analysis.

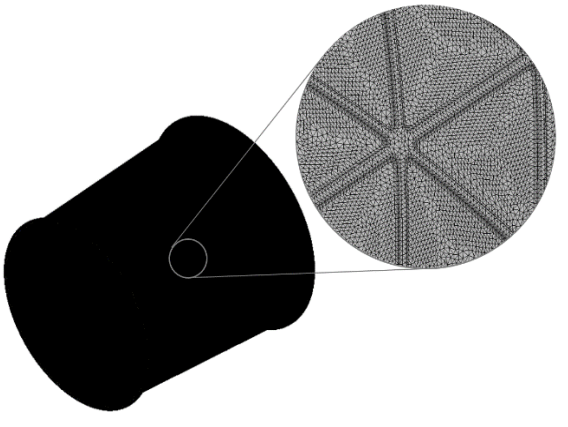

Fig. 5 Meshed lattice conical shell.

In order to converge the results of the analysis related to the lattice conical shell, the mesh independency study was performed for this shell (“Fig. 6”). In “Fig. 7”, the horizontal axis corresponds to the number of elements and the vertical axis corresponds to the maximum stresses on the lattice conical shell. The results show that the convergence of the analysis is acceptable. In the loading conditions section, the internal pressure force, the axial pressure force on the primary flange, and the vertical pressure force on the primary flange are applied (“Fig. 8”).

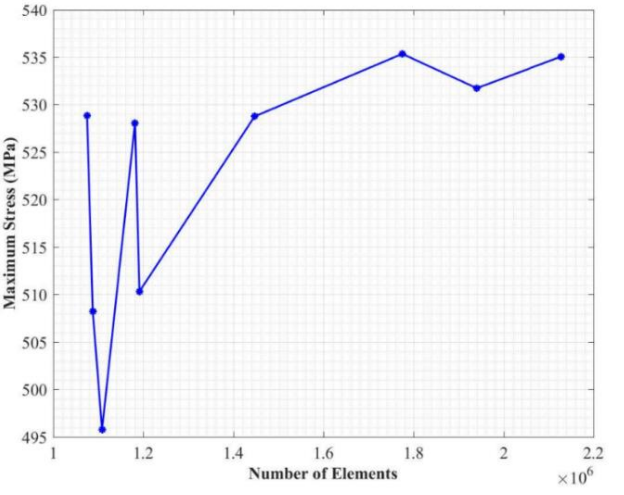

Fig. 6 Mesh independency study diagram for lattice conical shell.

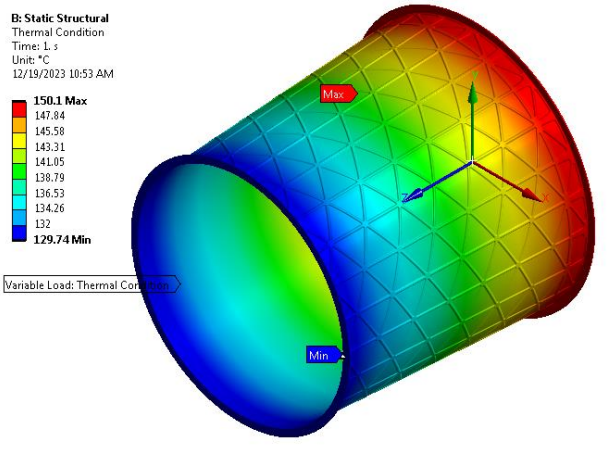

Fig. 7 The temperature gradient applied to the shell.

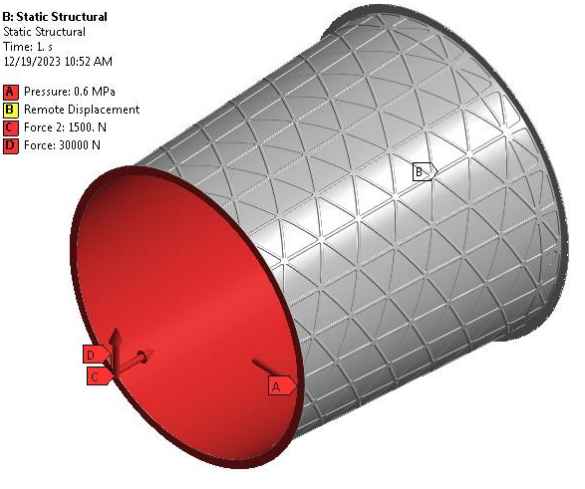

Fig. 8 Lattice conical shell under loading conditions.

Considering safety requirements, manufacturability, uncertainty in material strength, operating conditions, and possible defects in lattice shells, the value of internal pressure is considered with a safety factor of 2 (The value of internal pressure is 0.3 MPa, which becomes 0.6 MPa by considering the safety factor of 2). Also, the temperature gradient has been applied to the lattice conical shell ("Table 3"). The lattice conical shell is modeled in such a way that the heat source is adjoined to the large flange. As a result, the temperature in the large flange is higher and the temperature decreases as it moves away from the heat source ("Fig. 7"). In applying the boundary conditions, the outer surface of the conical end flange is under the remote displacement support condition, and all its degrees of freedom are set to zero.

Table 3 Mechanical loading and thermal conditions applied to the lattice conical shell

Applied Load	Value
Internal Pressure	0.6 MPa
Axial Compressive Force	30000 N
vertical compressive force	1500 N
Temperature Gradient	130-150 ℃

The final model of the lattice conical shell is finite element analysis after applying the loading conditions. The shell has been analyzed in terms of the equivalent stress value, maximum stress value, deformation, and necessary safety factor.

5 RESULTS

The finite element method is used to study the lattice conical shell under axis compressive, internal compressive, vertical compressive, and thermal gradient loads. In general, the aim of the finite element method of lattice conical shell is to provide a practical method to study the behavior of this structure.

The lattice conical shell has been analyzed under the mentioned loads. The lattice conical shell has been investigated in terms of equivalent stress and deformation. The results of finite element analysis are shown in "Figs. 9-15".

According to the figures and diagrams, the following results are deduced:

1. It can be seen that the maximum stress occurred at the intersection of the horizontal stiffeners and end flange and the minimum stress occurred at the flanges.
2. Considering that the internal pressure is applied to the lattice conical shell, the inside of the shell is uniform, but the outside of the shell has stiffeners and fillets, so the maximum stress outside the shell is more than the maximum stress inside the shell.
3. The maximum deformation was near the initial flange because the axial and vertical compressive loads were applied to this area. The minimum deformation is in the end flange because this part is under the remote displacement support condition.
4. The deformation in the radial direction is less than the deformation in the axial direction ("Fig. 13").
5. An increase in vertical force on the lattice conical shell causes an increase in the stress (Figure 15).
6. The maximum safety factor is on horizontal stiffeners and flanges.
7. The total mass of the system is about 41 kg.
8. The final minimum safety factor is about 2 and the model is acceptable for the desirable industrial conditions.

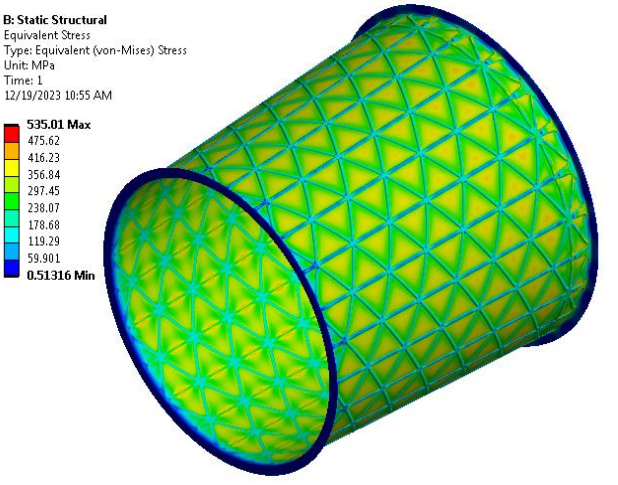

Fig. 9 The contour of the maximum stress on the lattice conical shell.

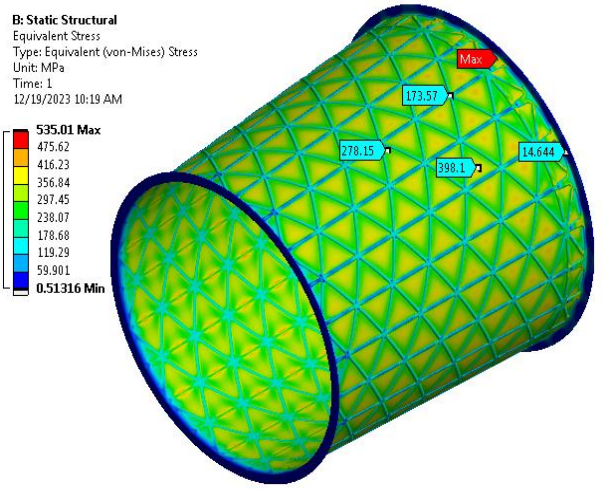

Fig. 10 Different values of stress on the lattice conical shell.

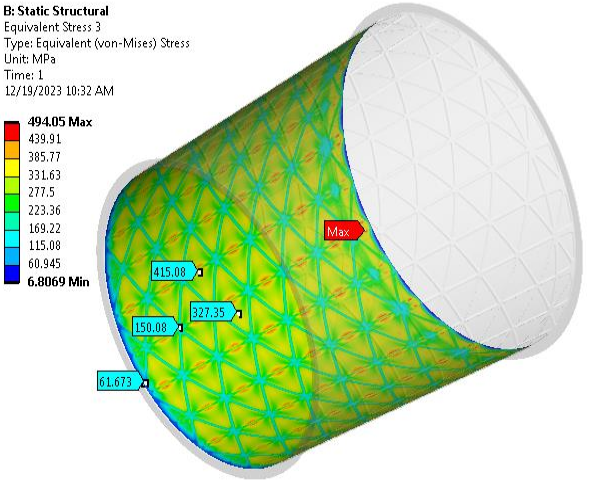

Fig. 11 The maximum stress contour on the inner surface of the lattice conical shell.

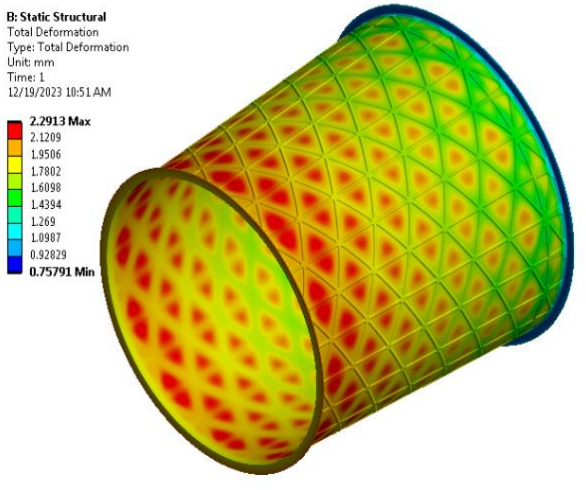

Fig. 12 Deformation contour of lattice conical shell under applied loads.

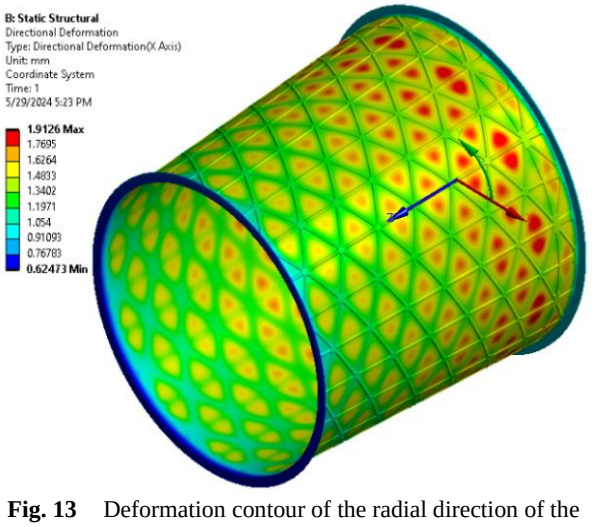

Fig. 13 Deformation contour of the radial direction of the lattice conical shell.

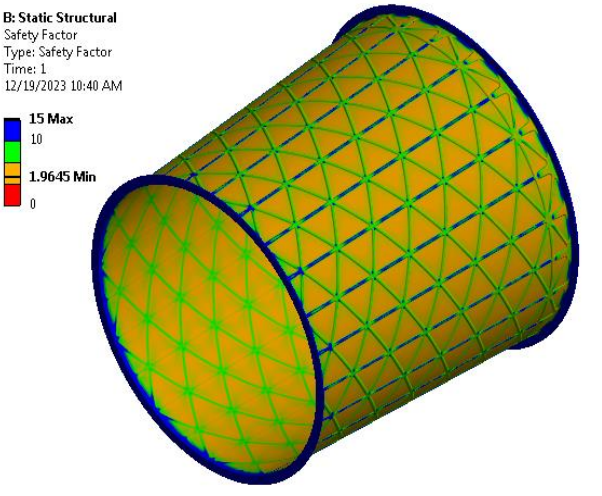

Fig. 14 Safety factor contour for lattice conical shell.

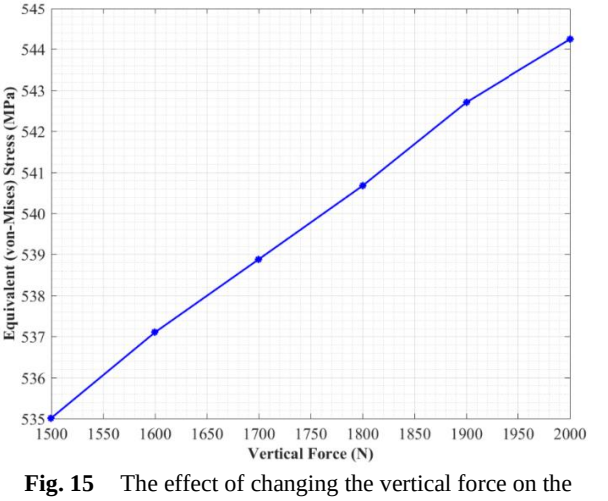

Fig. 15 The effect of changing the vertical force on the value of stress.

6 VALIDATIONS

To confirm the performed finite element method, the stress on the pressure vessel is investigated. The Pressure vessel is modeled in SolidWorks software (The dimensions of this Pressure vessel are equal to the dimensions of the lattice conical shell). The pressure vessel is subjected to internal pressure. The pressure vessel is implemented for finite element analysis in the ANSYS Workbench and its results are obtained ("Fig. 16"). Figure 17 shows that according to the linear Equation (1), the stress value (σ) increases with the increase of the radius (R).

$$\sigma(MPa) = (0.44 \times R) + 53.22 \quad (1)$$

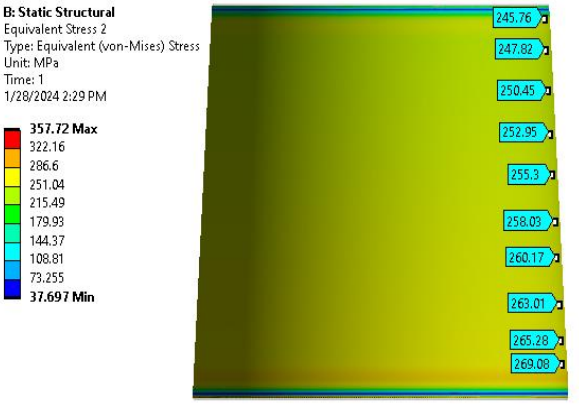

Fig. 16 The value of stress in different radii of the cone.

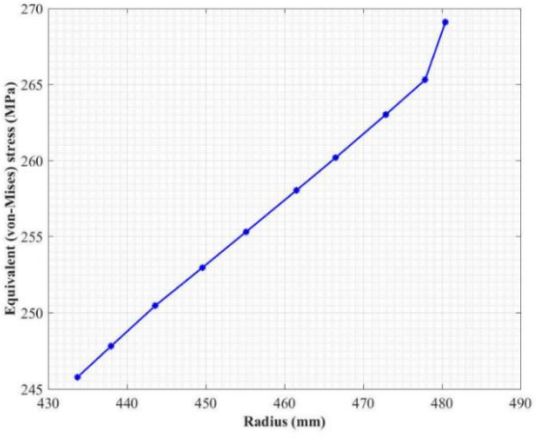

Fig. 17 Stress distribution diagram along the cone.

Therefore, the stress formula can also be used in pressure vessels. To prove the stress value obtained from the finite element analysis, The analytical solution of the pressure vessel is discussed. In the analytical method, the stress in each direction is according to "Fig. 18". Considering that the value of σ_3 is much smaller than the value of σ_2 and σ_1, then it is ignored.

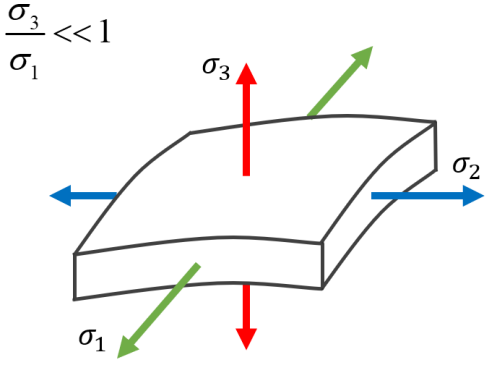

Fig. 18 Stress in coordinate Axis.

To obtain the stress value in the radial direction (σ_1), an element of the pressure vessel is considered ("Figs. 19 and 20).

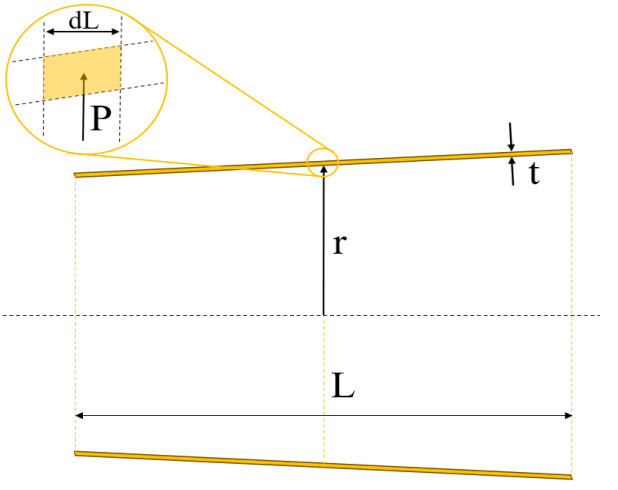

Fig. 19 Effective parameters in the pressure vessels (σ_1).

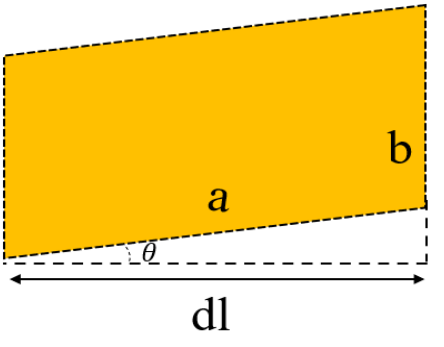

Fig. 20 Element of the pressure vessel.

The area of shell element is obtained from Equation (2):

$$A = ab\sin(\frac{\pi}{2} - \theta) = ab\cos\theta \quad (2)$$

The values of (a) and (b) in Equation (2) are equal to (Equation (3)):

$$a = \frac{dl}{\cos\theta}, b = t \quad (3)$$

By inserting the values of 3 in Equation (2), it is obtained:

$$A = t \times dl \quad (4)$$

The force of the element is obtained from Equation (5):

$$ElementForce = P \times (2t \times dl) \quad (5)$$

Because this shell has a thin thickness and this shell is under internal pressure and the strain vector is zero, the problem is solved in the form of plane stress. According to "Fig. 19", if an element of pressure vessels is considered, the equivalence Equation in the radial direction (σ_1) is equal to:

$$\sigma_1(2t\times dL)=P(2r\times dL) \tag{6}$$

The stress in the radial direction (σ_1) is obtained from Equation (7):

$$\sigma_1=\frac{Pr}{t} \tag{7}$$

Table 4 Values of effective parameters in pressure vessel

Parameter	Value
Internal Pressure (P)	0.6 MPa
Middle radius (r)	473×10^{-3} m
Slope of the Cone (θ)	3 deg
Length (L)	1 m
Thickness (t)	1×10^{-3} m

The value of stress in the radial direction on an element of pressure vessel is obtained, by putting the values ("Table 4") in Equation 7:

$$\sigma_1=\frac{0.6\times10^6\times473\times10^{-3}}{1\times10^{-3}}=283.8\times10^6\,Pa \tag{8}$$

To obtain the stress value in the longitudinal direction (σ_2), the element of the pressure vessel is considered ("Fig. 21").

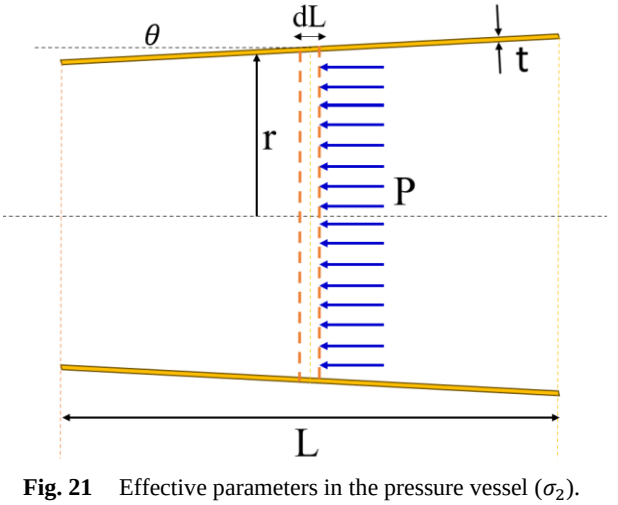

Fig. 21 Effective parameters in the pressure vessel (σ_2).

Static equilibrium is in the longitudinal direction (σ_2). The value of longitudinal (tensile) stress is equal to:

$$\sigma_2(2\pi\times rt)\times\cos\theta=\mathrm{P}\times(\pi\,\mathrm{r}^2) \tag{9}$$

The stress in the longitudinal direction (σ_2) is obtained from Equation (10):

$$\sigma_2=\frac{\mathrm{Pr}}{2t\times\cos\theta} \tag{10}$$

The value σ_2 is obtained, by substituting the values ("Table 4") into "Eq. (10)":

$$\sigma_2=\frac{0.6\times10^6\times473\times10^{-3}}{2\times(1\times10^{-3})\cos(3)}=142.09\times10^6\,Pa \tag{11}$$

According to Mohr's circle, since $\sigma_2<\sigma_1$, then the value of σ_1 is accepted as the final stress in the element ("Fig. 22").

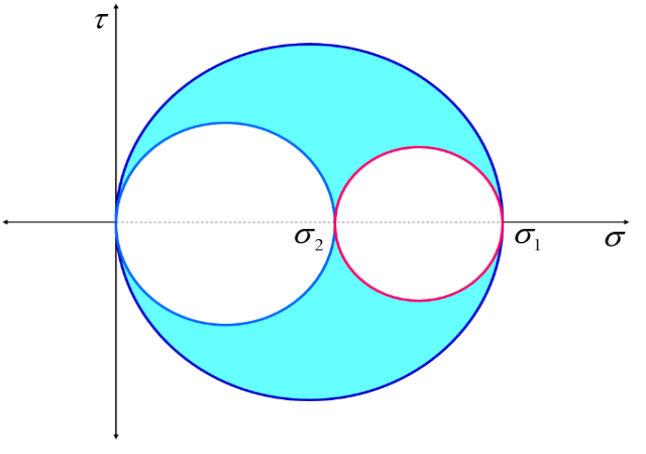

Fig. 22 Mohr's circle for (σ_1 ,σ_2).

In the finite element analysis, the stress value at the radius of 473×10^{-3} m is equal to 263.4×10^6 Pa, which is close to the value obtained from the analytical solution. The value of the Relative Error is equal to:

$$RE=\frac{(283.8\times10^6)-(263.4\times10^6)}{283.8\times10^6}=7.18\% \tag{12}$$

The results obtained from the analytical solution using the finite element method have a minor difference from the results obtained from the numerical solution, so it can be concluded that the numerical results of the lattice conical shell are acceptable.

7 CONCLUSIONS

In this study, the development of a generative algorithm related to the lattice conical shell and the modeling of this lattice conical shell under mechanical and thermal loads were discussed. To this purpose, an algorithm for the lattice conical shell has been developed in MATLAB software, which generates the stiffener pattern on the conical shell. Using this model, the lattice conical shell was modeled in SolidWorks software and analyzed for loading in ANSYS Workbench. The lattice structure reduced the total mass significantly, while the structure has acceptable resistance to mechanical loading and the final safety factor is acceptable.

1. The combination of ribs and strings is very resistant to loads.
2. The maximum stress is at the intersection of the horizontal stiffeners with the end flange. Considering that the safety factor of this part is acceptable, the modeling is reliable.
3. This structure can also be used in aerospace systems due to its low mass and high resistance. The design with minimal mass can have a significant effect on fuel reduction.
4. Whereas the safety factor of the final model is about 2 and the model is acceptable for desirable industrial conditions, the total system mass is about 41 kg.
5. Whereas the real internal pressure of the system is about 0.3 MPa, the system is designed for 0.6 MPa. This subject increases the total safety factor and reliability of the system.

REFERENCES

[1] Kim, T. D., Fabrication and Testing of Composite Isogrid Stiffened Cylinder, Composite Structures, Vol. 45, No. 1, 1999, pp. 1-6.

[2] G. Rahimi, G., Zandi, M., and Rasouli, S., Analysis of the Effect of Stiffener Profile on Buckling Strength in Composite Isogrid Stiffened Shell Under Axial Loading, Aerospace Science and Technology, Vol. 24, No. 1, 2013, pp. 198-203.

[3] Totaro, G., Local Buckling Modelling of Isogrid and Anisogrid Lattice Cylindrical Shells with Triangular Cells, Composite Structures, Vol. 94, No. 2, 2012, pp. 446-452.

[4] Jam, J. E., Noorabadi, M., Taghavian, H., and Namdaran, N., Design of Anis Grid Composite Lattice Conical Shell Structures, Researches and Applications in Mechanical Engineering, Vol. 1, No. 1, 2012, pp. 5-12.

[5] Kim, T. D., Fabrication and Testing of Thin Composite Isogrid Stiffened Panel, Composite Structures, Vol. 49, No. 1, 2000, pp. 21-25.

[6] Sorrentino, L., Marchetti, M., Bellini, C., Delfini, A., and Del Sette, F., Manufacture of High Performance Isogrid Structure by Robotic Filament Winding, Composite Structures, Vol. 164, 2017, pp. 43-50.

[7] Belardi, V. G., Fanelli, P., and Vivio, F., Design, Analysis and Optimization of Anisogrid Composite Lattice Conical Shells, Composites Part B: Engineering, Vol. 150, 2018, pp. 184-195.

[8] Hao, M., Hu, Y., Wang, B., and Liu, S., Mechanical Behavior of Natural Fiber-Based Isogrid Lattice Cylinder, Composite Structures, Vol. 176, 2017, pp. 117-123.

[9] Akl, W., El-Sabbagh, A., and Baz, A., Optimization of the Static and Dynamic Characteristics of Plates with Isogrid Stiffeners, Finite Elements in Analysis and Design, Vol. 44, No. 8, 2008, pp. 513-523.

[10] Li, M., Lai, C., Zheng, Q., Han, B., Wu, H., and Fan, H., Design and Mechanical Properties of Hierarchical Isogrid Structures Validated by 3D Printing Technique, Materials & Design, Vol. 168, 2019, pp. 107664.

[11] Totaro, G., Optimal Design Concepts for Flat Isogrid and Anisogrid Lattice Panels Longitudinally Compressed, Composite Structures, Vol. 129, 2015, pp. 101-110.

Int. J. Advanced Design and Manufacturing Technology, 2024, Vol. 17, No. 4, pp. 45-52

DOI: ***ISSN: 2252-0406*** ***https://admt.isfahan.iau.ir***

The Effect of using a Semi-Automatic Foam Cutting Machine on The Characteristics of Foam Patterns in The Lost Foam Casting

Sadegh Mirzamohammadi *, Abbas Abbasian
Department of Materials and Metallurgical Engineering, National University of Skills (NUS), Tehran, Iran
E-mail: s-mirzamohammadi@tvu.ac.ir, a-abbasian@tvu.ac.ir
*Corresponding author

Seyed Jalal Hashemi
Department of Mechanical Engineering, National University of Skills (NUS), Tehran, Iran
E-mail: j_hashemi@tvu.ac.ir

Received: 19 January 2016, Revised: 26 April 2016, Accepted: 10 May 2016

Abstract: In this research, a modern method for making foam patterns, which is one of the most important steps of casting with a lost foam pattern, has been used. A semi-automatic hot wire machine was built to cut and create foam patterns. Two types of foam patterns were prepared by manual method and cutting method with semi-automatic machine. The sizes of the obtained foam patterns were evaluated and the accuracy of each method in the production of foam patterns was compared. According to the density of the foam used in the experiments, the volume of the prepared patterns was obtained by manual and semi-automatic methods. The additional volume in the prepared patterns was calculated by both methods. The amount of economic losses caused by excess volumes was investigated. The results of the research determined that the accuracy of the sizes of the patterns prepared by the semi-automatic method was more than twice the accuracy of the patterns prepared by the manual method. The patterns prepared by the semi-automatic method had an additional volume of 1.9% compared to the volume of the original part. While the mentioned amount for foam patterns cut by the manual method was 9%. Therefore, the economic efficiency of casting parts using foam patterns made by semi-automatic method in terms of melting consumption for aluminum parts was 8% more than production parts using foam patterns made by manual method.

Keywords: Lost Foam Casting, Patterns, Precision, Semi-Automatic Foam Cutting

Biographical notes: Sadegh Mirzamohammadi is an assistant professor at the National University of Skills (NUS). He received his PhD from K. N. Toosi University of Technology in 2017. His current research focuses on surface engineering and composites and casting materials. **Abbas Abbasian** is a faculty member at the National University of Skills (NUS). He graduated in MSc degree from Hakim Sabzevari University in 2015. His current research focuses on casting methods and materials selection. **Seyed Jalal Hashemi** is an assistant professor at the National University of Skills (NUS). He received his PhD from Tarbiat Modarres University in 2014. His current research focuses on sheet metal forming and powder metallurgy.

Research paper

1 INTRODUCTION

Lost foam casting is a type of evaporative pattern casting process. This method is very similar to precision casting, except that foam is used instead of wax [1]. The main advantage of this method over precision casting (with wax) is the elimination of the melting step and removing the wax from the mold. This is possible by using the low melting temperature and very low density of the foam [2]. This method is used in casting aluminum, magnesium, gray, and ductile iron [3]. The lost foam casting process makes it possible to produce complex parts in a cheaper way [4]. In common methods, cores are needed to create internal cavities, and the use of the lost foam method eliminates this need. In addition, this casting process is capable of producing parts with excellent surface smoothness [5]. This process does not require an exit angle. Therefore, the mold does not have any slit lines and this leads to no pleats. The absence of pleats and the absence of a slope for the exit of the pattern causes the reduction or elimination of polishing operations and final operations (such as heat treatment, machining, etc.). Reducing or eliminating the final casting operations reduces the amount of wastage and material waste during the process. This also leads to a reduction in the total cost [6]. Figure 1 shows an example of a complex piece produced by the lost foam method.

Fig. 1 Complex piece produced by the lost foam method.

In lost foam casting, patterns are made of expanded polystyrene (foam) and placed in sand without glue [7]. The chemical composition of foam and the schematic of foam production steps are shown in "Fig. 2". One of the most important advantages of using a foam pattern is the elimination of the core in the molding process [8]. The desired pattern is exactly the same as the part in terms of shape and size and is made of foam. The final pattern may consist of one or more pieces that are finally glued together to create a unified pattern. The feeding and runner systems are also made of foam and are attached to the pattern [9].

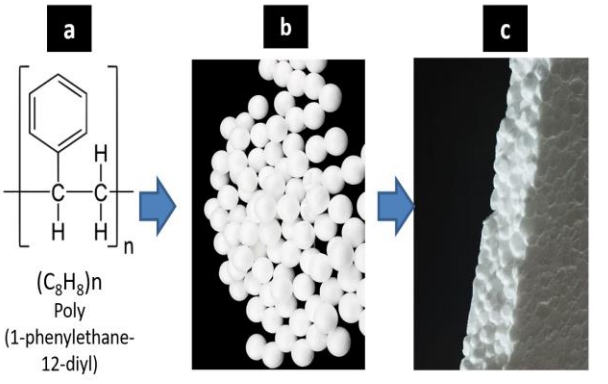

Fig. 2 (a): The chemical composition of foam, (b): Foam balls, and (c): Foam sheet.

Before putting the foam into the mold, the foams are coated [10]. The most important purpose of using the coating is to keep the sand and prevent it from collapsing [11]. Applying the coating also keeps the heat in the melt and increases its fluidity. These coatings maintain dimensional accuracy by preventing the shape of the foam pattern from changing during molding and vibration [12]. The chemical composition of the coating includes a powder, a refractory material, an adhesive, and a suspending solvent. Refractory material usually consists of silica, alumina, zinc oxide, chromite, and aluminosilicates such as mullite and pyrophyllite [13]. The resulting coating is in the form of a slurry. This coating is applied to the pattern through dipping, spraying, or painting with a pen. The coating is applied to the pattern in several steps. The drying process is usually done at a temperature of 50 to 60 °C and in a dryer for 24 hours. The thickness of the coating is usually about 0.25 to 0.5 mm [14].

After finishing the process of coating the patterns, the sample is placed inside the copes. The cope is filled with free-flowing dry sand containing carbon and without glue [2]. When pouring sand around the patterns, the whole system vibrates in three directions. This vibration is because the sand completely surrounds the pattern and fills all the holes in the piece [12]. After molding, pouring molten material into the mold causes the foam pattern to evaporate completely. The use of low-density polystyrene grains in the preparation of a foam pattern causes the amount of gas resulting from foam evaporation to decrease [2].

The use of lost foam casting is increasing. Currently, Tractor Sazi Casting Company uses this method to produce intermediate gearbox, tractor gearbox and all kinds of axles. A statistic obtained from the applied growth of this casting method in China is shown in "Fig. 3".

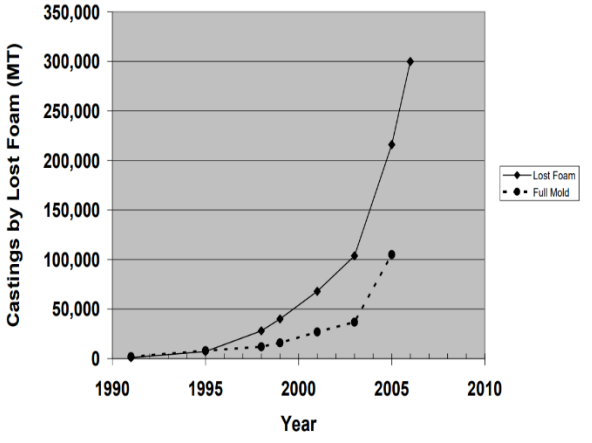

Fig. 3 Comparison of the tonnage of production of parts by conventional casting methods compared to the lost foam method in China [6].

Many different alloys are cast by the lost foam method and this method can have a very favorable effect on the obtained mechanical properties. The casting of Mg-Gd-Y-Zr alloys with this method has caused the maximum ultimate tensile strength to reach 285 MPa [3]. In the research of Xiao et al., it has been shown that the mechanical properties of gray cast iron can be improved using the lost foam method [15]. Jiang et al. have shown in their research that the pressure in the lost foam casting method will have a great impact on the quality of the part coming out of the mold [16]. The effective parameters in the lost foam process are very diverse and a lot of research has been done on this issue [14], [17].

Fig. 4 A hot knife that is used manually in making foam patterns.

One of the most important factors affecting the quality of the final piece is the quality of the foam pattern used in molding. Manual cutting is the first method used in making these foam patterns. However, it is clearly known that this method can have errors. For manual cutting, a variety of tools, including a hot knife, have also been used, as shown in "Fig. 4". Using a mechanical method and a foam moving machine to cut the foams can increase the accuracy in preparing foam patterns and increase economic efficiency. Little research has been done on the construction of semi-automatic cutting machines and their impact on the last foam casting. For this reason, in this research, the construction and use of a semi-automatic machine for cutting foam patterns were targeted. By making a semi-automatic machine for cutting foams, it was possible to compare foam patterns prepared by the semi-automatic method and manual method. In addition, the effect of using a semi-automatic hot wire machine on the characteristics of foam patterns, including the volume of the prepared pattern, casting, and economic losses, is investigated.

2 MATERIAL AND METHODS

In order to make a semi-automatic hot wire cutting machine, first a steel plate (10 x 15 cm) was prepared. Four steel belts with a length of 32 cm were cut. The steel plate was welded to the four mentioned belts. The above operation results in the construction of movable arms. Two prepared bearings were installed on the transmission shafts. The bearing used is shown in "Fig. 5". By means of screws, the bearings were connected to the plate and the movable arm. This action causes the longitudinal movement of the mobile arm and creates a rail (wing bush) for the movement of the arms.

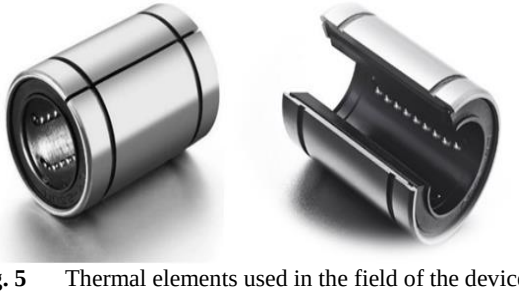

Fig. 5 Thermal elements used in the field of the device.

Then a chain with number 25 was installed on the engine sprocket. By connecting the mentioned system to the metal plate, the movement of moving arms is provided by a three-position switch and a driver. The L-shaped arm is connected to the table through a screw, and two movable rails are placed on the horizontal and vertical beams of the L-shaped arm to change the angle of the element. The elements were connected to the current source using a built-in dimmer. The dimmer controls the heat required for cutting. This heat can be adjusted according to the density of the foam and the speed of movement of the longitudinal arm. "Table 1" shows the components of the semi-automatic hot wire cutting machine. The thickness of the wires depends on the application environment and varies from 0.32 to 6 mm. The wire used in these experiments is shown in "Fig. 6".

Table 1 The components of the semi-automatic hot wire cutting machine

Num.	Component	Num.	Component
1	desk	9	Trans shaft 16 mm
2	Steel (plate - corner - belt)	10	LME bearing
3	Chain number 25	11	22 teeth chain wheel
4	three positioned rail	12	Element tension mechanism
5	Foam retaining clips	13	Dimmer (5000)
6	12 volt DC motor	14	PCDM1 driver
7	12V/10A adapter	15	Thermal element (thick 0.32 mm)
8	Two-stage and three-stage key	16	terminal

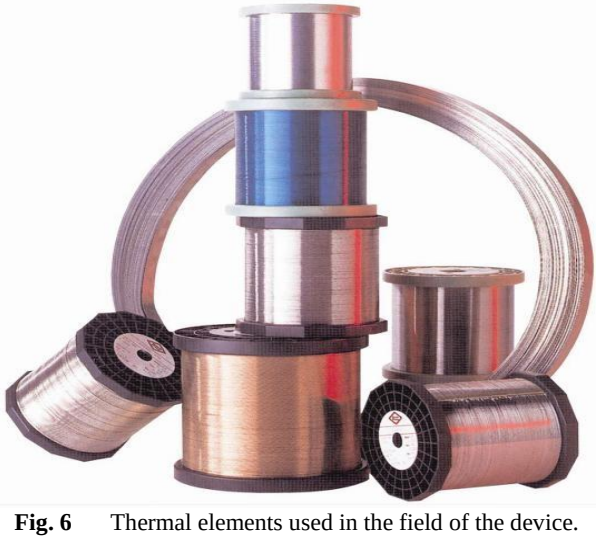

Fig. 6 Thermal elements used in the field of the device.

These used elements have the property that they can withstand very large currents. The main material of the elements is nichrome and they have different powers. Most nichrome elements are made with an 80/20 composition (80% nickel, 20% chromium). This material is desirable in the sense that it has high electrical resistance and when it is first heated, it forms a sticky layer of chromium oxide on itself, which prevents internal parts from oxidizing and burning or breaking. It should be mentioned that the thickness of the used wire is directly related to the density of the used foam and the dimensions of the pattern. By increasing the thickness of the wire, the amperage of the device should also be increased.

In the manual cutting method, all cutting operations are done with the help of the operator and through hand movements. For example, for the longitudinal cuts of the foam block, the process is guided with the help of a guide plate. The cutting action is based on the predetermined size and dimensions in the foam. Also, in circular cuts (cylindrical cutting), cutting is done by determining the center and radius of the desired cylinder and by moving the hand around the axis of rotation. In the semi-automatic cutting method, longitudinal cuts are made with the help of mechanisms built into the machine. In the automatic cutting operation, the moving arms that are connected to the rail are connected to the motor by a chain. When the motor is activated and the speed is set by the driver, the arms are guided to the beginning and end of the table. Foam patterns are made by manual and semi-automatic methods. In both methods, the general steps of making a foam pattern are shown in "Fig. 7".

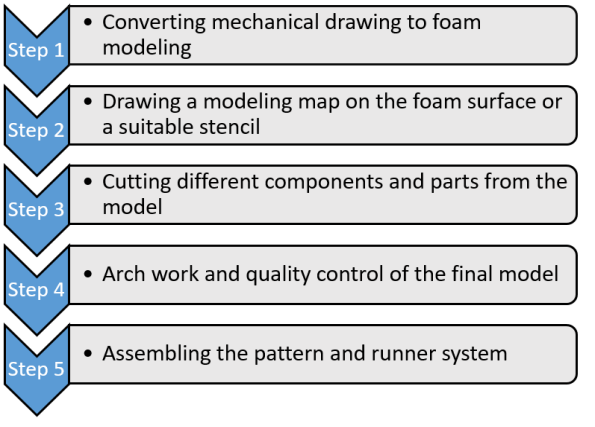

Fig. 7 Flowchart of the general steps of making foam patterns with semi-automatic and manual methods.

3 RESULTS AND DISCUSSION

3.1. Semi-Automatic Foam Cutting Hot Wire Machine

The trans shaft, bearing, and chain were placed in the longitudinal movement mechanism. As seen in "Fig. 8", the chain used in the semi-automatic cutting machine has technical number 25 and the length of the chain is 236 cm. The chain is attached to the support plate of the movable arms by three small screws, one side of the chain is mounted on the DC motor sprocket, and the other side is mounted on an idler sprocket. With the activation of the engine and the rotation of the chain wheel, the rotational force of the engine is transferred to

the chain and causes the longitudinal movement of the mobile arms.

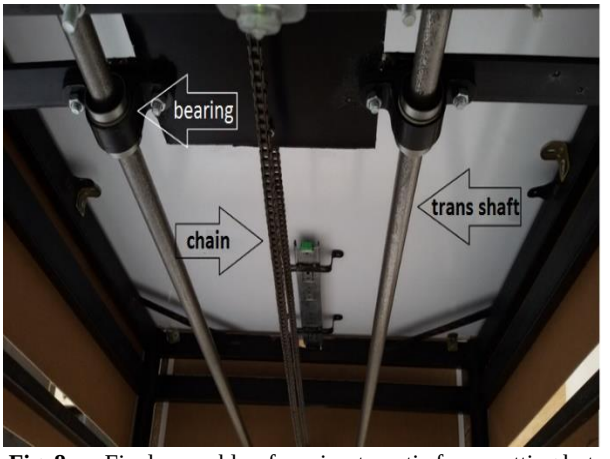

Fig. 8 Final assembly of semi-automatic foam cutting hot wire machine.

As shown in "Fig. 9", a semi-automatic foam cutting hot wire machine was built. Among the characteristics of the manufactured machine, the very low price of the above machine can be mentioned compared to similar machines such as the CNC machine. Despite this low price, the accuracy of this machine is very high compared to manual cutting by the operator. In addition to the mentioned features, this device can cut large objects and has a low maintenance cost, ease of use, and the ability to adjust the temperature of the wire element and semi-automation.

Fig. 9 Final assembly of semi-automatic foam cutting hot wire machine.

In this device, after the main key is pressed, the system allows 220V electricity to enter the terminal in the device. The terminal of the device transfers and changes the input power to the dimmer and adapter. The dimmer gives electric current to the element and as a result, the electric energy is converted into thermal energy. Also, the operator performs the semi-automatic cutting operation by placing the foam between the two moving clamps and activating the motor key. In order to cut cylindrical objects by specifying the center of the foam and placing it in the designed place (flange), the operator performs cylindrical cutting by rotating the foam.

3.2. Preparing Foam Patterns and Comparing the Patterns Obtained by Semi-Automatic and Manual Methods

Two foam patterns were prepared from two different pieces using a semi-automatic machine and a manual method. Figure 10 shows the image of these two examples of foam patterns. The accuracy of the foam patterns prepared using manual hot wire cutting methods and semi-automatic hot wire cutting machine is shown in the graphs drawn in "Fig. 11". Paying attention to the results obtained in these two graphs shows that the error percentage in the size obtained in the foam patterns that were prepared by semi-automatic method is much lower than the sizes obtained in the foam patterns that were prepared by the manual method.

Fig. 10 View of two foam patterns made from two different castings.

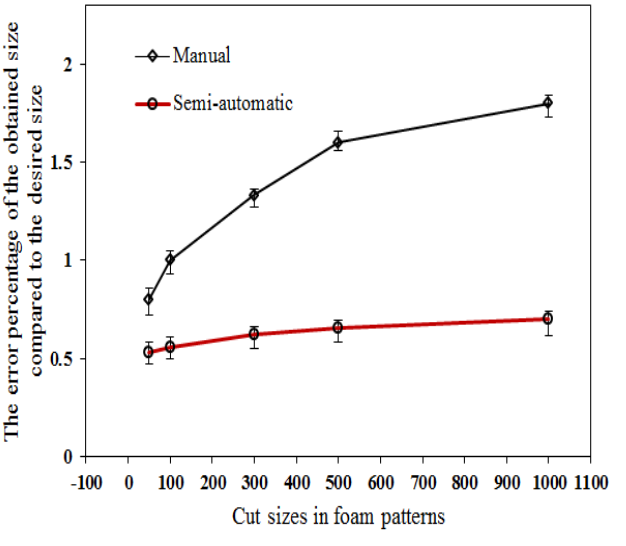

Fig. 11 Graphs of the percentage of mistakes that occurred in the preparation of foam patterns with sizes of 50 to 1000 mm by semi-automatic and manual methods.

In cutting 100 mm using the manual method, an average error of 1% was observed, but in cutting 100 mm using the semi-automatic method, the average error percentage was reduced to 0.56%.

Observing the changes in the error percentage in the trend of the graphs shows that with the increase in the size of the foams and in other words the size required for the foam patterns, the possibility of increasing the error percentage in the manual method increases at a very significant rate. In this way, in cutting a foam pattern with a size of 1000 mm by manual method, the error percentage increases to about 1.8%. While this value for the semi-automatic method is 0.7%.

Therefore, in general, it can be stated that the use of semi-automatic method in the preparation of foam patterns used in casting industries can reduce the error percentage from 1.8 to 0.7% (almost half), and will increase the accuracy of the preparation of foam patterns by more than two times.

In the following, the percentage of additional volume created in the foam patterns prepared by two semi-automatic and manual methods was calculated and the results are shown in "Fig. 12". As can be seen in the diagrams of the mentioned figure, the percentage of additional volume to the volume of the piece in foam patterns by manual method is 9%. This amount of loss is reduced to 1.9% by using the method of semi-automatic hot wire cutting machine. This additional volume reduction in foam patterns can have a significant impact on the cost of parts produced by the method of lost foam casting.

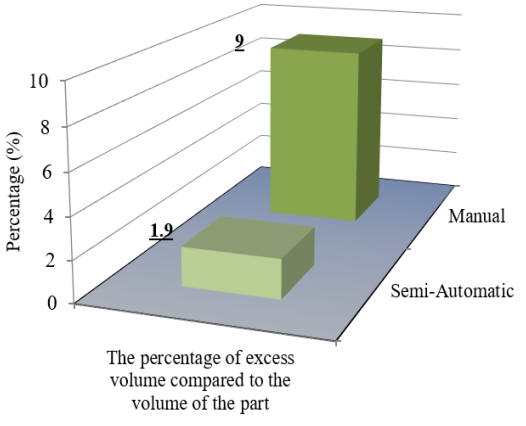

Fig. 12 The percentage of additional volume of foam patterns prepared by semi-automatic and manual methods compared to the volume of the piece.

In the manual method of making foam patterns, patterns are usually cut in larger sizes [18], because the parts should not be smaller than the size required for casting. If they are cast larger, it is possible to machine them to life-size [19-20]. Therefore, in methods of preparing foam patterns that are more accurate in cutting, aluminum consumption and machining costs will be reduced. The comparison of the weight of aluminum used to produce a piece with a volume of 2000 cm^3 in the methods of preparing a semi-automatic and manual foam pattern was done in this research. Figure 13 shows a comparison of the final weight of aluminum used in the two mentioned methods. As can be seen in the figure, the weight of aluminum used in the case of foams cut by manual method is 5.9 kg, but in the case of foams cut by semi-automatic method, this weight is reduced to 5.5 kg. Therefore, by replacing the semi-automatic method instead of the manual method, in the production of casting foams, the amount of aluminum ingots consumed is reduced to 8%. So, using a semi-automatic cutting machine can be a suitable method to achieve casting with higher precision.

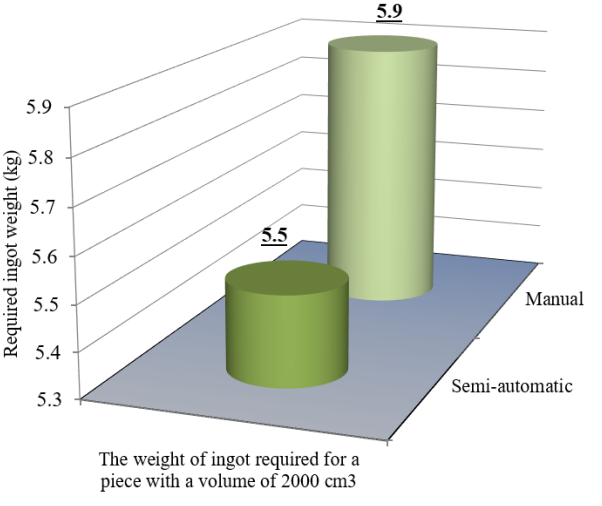

Fig. 13 The weight of aluminum ingot required to produce a piece with a volume of 8000 cm3 in semi-automatic and manual foam preparation methods.

4 CONCLUSIONS

In this research, a semi-automatic foam cutting hot wire machine was made for the first time and used to prepare foam patterns of lost foam casting. Foam patterns prepared by semi-automatic method and manual method were compared and their important and effective features were studied in the field of casting. The following results are derived from this study.

• The accuracy of the sizes of the patterns prepared by the semi-automatic method was more than twice the accuracy of the patterns prepared by the conventional manual method. In a 100 mm cut by manual method, an average of 1% error occurred, but the same cut by semi-

automatic method reduced the error percentage to 0.56%.

• The patterns prepared by the semi-automatic method had an additional volume of 1.9% more than the volume of the original part. While the mentioned amount for foam patterns cut manually was 9%.

• The economic efficiency of casting parts using foam patterns made by semi-automatic method in terms of melting consumption for aluminum parts was 8% higher than the production parts using foam patterns made by manual method.

REFERENCES

[1] Barone, M. R., Caulk, D. A., A Foam Ablation Model for Lost Foam Casting of Aluminum, International Journal of Heat and Mass Transfer, Vol. 48, No. 19–20, 2005, pp. 4132–4149, doi: 10.1016/j.ijheatmasstransfer.2005.03.031.

[2] Basso, A., Toda-Caraballo, I., San-Martín, D., and Caballero, F. G., Influence of Cast Part Size on Macro- and Microsegregation Patterns in A High Carbon High Silicon Steel, Journal of Materials Research and Technology, Vol. 9, No. 3, 2020, pp. 3013–3025, doi: 10.1016/j.jmrt.2020.01.052.

[3] Brown, J., Foseco Ferrous Foundryman's Handbook. Elsevier Science, 2000.

[4] Chen, H. Z., Shan, Z. De, and Dong, H. Z., Research of Foam Pattern Processing for Lost Foam Casting, International Conference on Process Equipment, Mechatronics Engineering and Material Science, Vol. 331, 2013, pp. 600–603, doi: 10.4028/www.scientific.net/AMM.331.600.

[5] Guler, K. A., Acar, S., Lost Foam Casting of Metallic Parts and Structures, In F. G. Caballero (Ed.), Encyclopedia of Materials: Metals and Alloys, Elsevier, 2022, pp. 73–86, doi: 10.1016/B978-0-12-819726-4.00008-9.

[6] Guler, K. A., Kisasoz, A., and Karaaslan, A., Effects of Pattern Coating and Vacuum Assistance on Porosity of Aluminium Lost Foam Castings, Russian Journal of Non-Ferrous Metals, Vol. 55, No. 5, 2014. pp. 424–428. doi: 10.3103/S1067821214050113.

[7] Jafari, H., Idris, M. H., and Shayganpour, A., Evaluation of Significant Manufacturing Parameters in Lost Foam Casting of Thin-Wall Al-Si-Cu Alloy Using Full Factorial Design of Experiment, Transactions of Nonferrous Metals Society of China (English Edition), Vol. 23, No. 10, 2013, pp. 2843–2851, doi: 10.1016/S1003-6326(13)62805-8.

[8] Jiang, W., Fan, Z., Liao, D., Liu, D., Zhao, Z., and Dong, X., Investigation of Microstructures and Mechanical Properties of A356 Aluminum Alloy Produced by Expendable Pattern Shell Casting Process with Vacuum and Low Pressure, Materials and Design, Vol. 32, No. 2, 2011, pp. 926–934, doi: 10.1016/j.matdes.2010.08.015.

[9] Kannan, P., Biernacki, J. J., and Visco, D. P., A Review of Physical and Kinetic Models of Thermal Degradation of Expanded Polystyrene Foam and Their Application to The Lost Foam Casting Process, Journal of Analytical and Applied Pyrolysis, Vol. 78, No. 1, 2007, pp. 162–171, doi: 10.1016/j.jaap.2006.06.005.

[10] Karimian, M., Ourdjini, A., Hasbullah Idris, M., and Jafari, H., Effect of Pattern Coating Thickness on Characteristics of Lost Foam Al-Si-Cu Alloy Casting, Transactions of Nonferrous Metals Society of China (English Edition), Vol. 22, No. 9, 2012, pp. 2092–2097, doi: 10.1016/S1003-6326(11)61433-7.

[11] LI, J., Chen, R., and Ke, W., Microstructure and Mechanical Properties of Mg-Gd-Y-Zr Alloy Cast by Metal Mould and Lost Foam Casting, Transactions of Nonferrous Metals Society of China, Vol. 21, No. 4, 2011, pp. 761–766, doi; 10.1016/S1003-6326(11)60777-2.

[12] Liu, X. J., Overfelt, R. A., and Bhavnani, S. H., The Effects of Foam Density and Metal Velocity on The Heat and Mass Transfer in The Lost Foam Casting Process, Proceedings of the ASME Summer Heat Transfer Conference, 2003, pp. 317–323, doi: 10.1115/ht2003-47504.

[13] Nicoletto, G., Anzelotti, G., and Konečná, R., X-Ray Computed Tomography Vs, Metallography for Pore Sizing and Fatigue of Cast Al-Alloys, Procedia Engineering, Vol. 2, No. 1, 2010, pp. 547–554. doi: 10.1016/j.proeng.2010.03.059.

[14] Paramasivam, K., Vijay Anand, M., and Sambathkumar, M., Investigation of Optimum Process Parameter of Lost Foam Casting of A356/SiC Metal Matrix Composite, Materials Today: Proceedings, Vol. 47, 2021, pp. 4801–4806, doi: 10.1016/j.matpr.2021.06.035.

[15] Sands, M., Shivkumar, S., Influence of Coating Thickness and Sand Fineness on Mold Filling in The Lost Foam Casting Process, Journal of Materials Science, Vol. 38, No. 4, 2003, pp. 667–673, doi: 10.1023/A:1021859523363.

[16] Shayegh, J., Hossainpour, S., Rezaei, M., and Charchi, A., Developing a New 2D Model for Heat Transfer and Foam Degradation in EPS Lost Foam Casting (LFC) Process, International Communications in Heat and Mass Transfer, Vol. 37, No. 9, 2010, pp. 1396–1402, doi: 10.1016/j.icheatmasstransfer.2010.07.015

[17] Sun, D., An Overview of Lost Foam Casting Technology Development in China. AFS Transactions, American Foundry Society, Vol. 08–035, No. 14, 2008, pp. 1–8.

[18] Wang, L., Limodin, N., El Bartali, A., Witz, J. F., Seghir, R., Buffiere, J. Y., and Charkaluk, E., Influence of Pores on Crack Initiation in Monotonic Tensile and Cyclic Loadings in Lost Foam Casting A319 Alloy by Using 3D In-Situ Analysis, Materials Science and Engineering: A, Vol. 673, 2016, pp. 362–372, doi: 10.1016/j.msea.2016.07.036.

[19] Xiao, B., Fan, Z., Jiang, W., Liu, X., Long, W., and Hu, Q., Microstructure and Mechanical Properties of

Ductile Cast Iron in Lost Foam Casting with Vibration, Journal of Iron and Steel Research, International, Vol. 21, No. 11, 2014, pp. 1049–1054, doi: 10.1016/S1006-706X(14)60182-5.

[20] Zhao, Z., Fan, Z. T., Jiang, W. M., and Dong, X. P., Microstructural Evolution of Mg9AlZnY Alloy with Vibration in Lost Foam Casting During Semi-Solid Isothermal Heat Treatment, Transactions of Nonferrous Metals Society of China (English Edition), Vol. 20, No. 3, 2010, pp. 768–773, doi: 10.1016/S1003-6326(10)60579-1.